




BRAIN COMMUNICATIONS

Small fibre neuropathy in Fabry disease: a human-derived neuronal *in vitro* disease model and pilot data

Thomas Klein,^{1,*}  Julia Grüner,^{1,*} Maximilian Breyer,¹ Jan Schlegel,^{2,†} Nicole Michelle Schottmann,¹ Lukas Hofmann,¹ Kevin Gauss,³ Rebecca Mease,³ Christoph Erbacher,¹ Laura Finke,¹ Alexandra Klein,¹ Katharina Klug,¹ Franziska Karl-Schöller,¹ Bettina Vignolo,¹ Sebastian Reinhard,² Tamara Schneider,^{4,‡} Katharina Günther,^{5,§} Julian Fink,⁶ Jan Dudek,⁷  Christoph Maack,⁷ Eva Klopocki,⁴ Jürgen Seibel,⁶ Frank Edenhofer,^{5,§} Erhard Wischmeyer,^{8,**} Markus Sauer² and  Nurcan Üçeyler^{1,9}

* These authors contributed equally to this work.

† Present address: Department of Women's and Children's Health, Karolinska Institutet, 17177 Stockholm, Sweden.

‡ Present address: Institute for Biology and Environmental Science, University of Oldenburg, 26129 Oldenburg, Germany.

§ Present address: Institute of Molecular Biology & CMBI, University of Innsbruck, 6020 Innsbruck, Austria.

** Present address: Cellular Neurophysiology, Bielefeld University, Medical Faculty Ostwestfalen-Lippe, 33615 Bielefeld, Germany.

Acral burning pain triggered by fever, thermal hyposensitivity and skin denervation are hallmarks of small fibre neuropathy in Fabry disease, a life-threatening X-linked lysosomal storage disorder. Variants in the gene encoding alpha-galactosidase A may lead to impaired enzyme activity with cellular accumulation of globotriaosylceramide. To study the underlying pathomechanism of Fabry-associated small fibre neuropathy, we generated a neuronal *in vitro* disease model using patient-derived induced pluripotent stem cells from three Fabry patients and one healthy control. We further generated an isogenic control line via gene editing. We subjected induced pluripotent stem cells to targeted peripheral neuronal differentiation and observed intra-lysosomal globotriaosylceramide accumulations in somas and neurites of Fabry sensory neurons using super-resolution microscopy. At functional level, patch-clamp analysis revealed a hyperpolarizing shift of voltage-gated sodium channel steady-state inactivation kinetics in isogenic control neurons compared with healthy control neurons ($P < 0.001$). Moreover, we demonstrate a drastic increase in Fabry sensory neuron calcium levels at 39°C mimicking clinical fever ($P < 0.001$). This pathophysiological phenotype was accompanied by thinning of neurite calibres in sensory neurons differentiated from induced pluripotent stem cells derived from Fabry patients compared with healthy control cells ($P < 0.001$). Linear–nonlinear cascade models fit to spiking responses revealed that Fabry cell lines exhibit altered single neuron encoding properties relative to control. We further observed mitochondrial aggregation at sphingolipid accumulations within Fabry sensory neurites utilizing a click chemistry approach together with mitochondrial dysmorphism compared with healthy control cells. We pioneer pilot insights into the cellular mechanisms contributing to pain, thermal hyposensitivity and denervation in Fabry small fibre neuropathy and pave the way for further mechanistic *in vitro* studies in Fabry disease and the development of novel treatment approaches.

1 Department of Neurology, University Hospital Würzburg, 97080 Würzburg, Germany

2 Department of Biotechnology and Biophysics, University of Würzburg, 97074 Würzburg, Germany

3 Medical Biophysics, Institute for Physiology and Pathophysiology, Heidelberg University, 69120 Heidelberg, Germany

4 Institute for Human Genetics, University of Würzburg, 97074 Würzburg, Germany

5 Institute of Anatomy and Cell Biology, University of Würzburg, 97070 Würzburg, Germany

Received October 10, 2023. Revised January 24, 2024. Accepted March 15, 2024. Advance access publication April 3, 2024

© The Author(s) 2024. Published by Oxford University Press on behalf of the Guarantors of Brain.

This is an Open Access article distributed under the terms of the Creative Commons Attribution License (<https://creativecommons.org/licenses/by/4.0/>), which permits unrestricted reuse, distribution, and reproduction in any medium, provided the original work is properly cited.

6 Institute of Organic Chemistry, University of Würzburg, 97074 Würzburg, Germany

7 Comprehensive Heart Failure Center CHFC, University Hospital Würzburg, 97080 Würzburg, Germany

8 Institute of Physiology, University of Würzburg, 97070 Würzburg, Germany

9 Würzburg Fabry Center for Interdisciplinary Therapy (FAZIT), University Hospital Würzburg, 97080 Würzburg, Germany

Correspondence to: Nurcan Üçeyler, MD

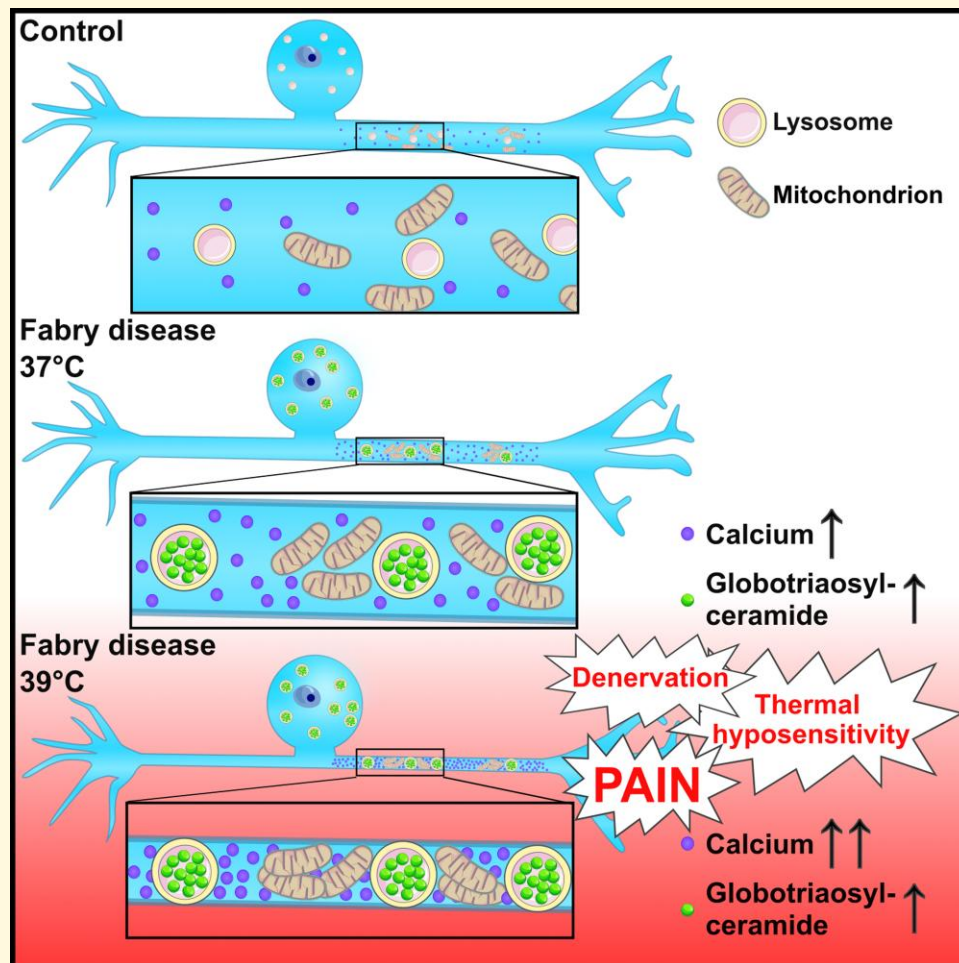
Department of Neurology, University Hospital Würzburg

Josef-Schneider-Str. 11, 97080 Würzburg, Germany

E-mail: ueceyler_n@ukw.de

Keywords: Fabry disease; globotriaosylceramide; induced pluripotent stem cells; disease model; lysosomes

Graphical Abstract



Introduction

Fabry disease is an X-linked lysosomal storage disorder that is caused by variants in the gene encoding alpha-galactosidase A (*GLA*).¹ Impairment of *GLA* activity results in cellular accumulation of sphingolipids, mainly globotriaosylceramide (Gb3).² The clinical phenotype spans a spectrum from classic Fabry disease, which is an age-dependent multi-organ disorder starting in early childhood, to late-onset symptom

manifestation in adulthood and with often milder symptoms. The main neurological manifestation of Fabry disease is small fibre neuropathy,³ which is characterized by episodic acral and triggerable burning pain, thermal hyposensitivity and peripheral denervation both in men and women.⁴

The pathophysiology of small fibre neuropathy in Fabry disease is incompletely understood. Studies in Fabry animal models such as the *GLA* knockout (KO) mouse⁵ show high caspase activity in sensory neurons and altered ion channel

function.⁶ Pain-related ion channels, such as members of the transient receptor potential vanilloid family and the family of voltage-gated sodium channels, are dysregulated.⁷ Further, gene expression related to lysosomes and ceramide metabolism is upregulated, whereas immune-related pathways are downregulated in *GLA* KO mice compared with wildtype.^{8,9} Although literature on the intracellular signaling pathways is sparse, a link between Ca^{2+} homeostasis and Fabry-associated symptoms has been proposed in murine sensory neurons¹⁰ and human cardiomyocytes derived from induced pluripotent stem cells (iPSC).¹¹ Incubation of murine dorsal root ganglia (DRG) with lyso-Gb3, the deacylated form of Gb3, led to a transient increase in cytosolic Ca^{2+} levels. Also, the Ca^{2+} -activated potassium channel KCa 3.1 was suggested to play a role in the pathogenesis of Fabry disease.¹² However, there are hardly any data available on the mechanisms how functional alterations of cellular Gb3 may lead to Fabry pathophysiology in a human model. To comprehensively study these mechanisms in patients, human sensory neurons are needed, which are not easily accessible *in vivo*.

Generation of sensory neurons from somatic cells via iPSC developed into a potent strategy to overcome this methodological roadblock.^{13,14} Multi-dimensional analysis of patient-derived sensory neurons provides in-depth insight into the molecular mechanisms underlying pain and sensory disturbance^{15,16} and paves the way for personalized treatment approaches.¹⁷⁻¹⁹ We pioneer a human *in vitro* model for Fabry disease and provide first evidence that *GLA* impairment is associated with altered neuronal properties as potential basis of small fibre neuropathy with pain, thermal hyposensitivity and peripheral denervation. Our study is the first to provide pilot data linking neuronal pathology with symptoms and signs of Fabry patients, opening avenues of unprecedented perspectives for future management of this life-threatening disease.

Materials and methods

Subjects

Our study was approved by the Würzburg Medical Faculty Ethics Committee (#135/15). Study participants gave written informed consent before inclusion, and subjects' consent was obtained according to the Declaration of Helsinki. We enrolled three patients (two men and one woman) with genetically approved Fabry disease in 2015 and 2016 via the Würzburg Fabry Center for Interdisciplinary Therapy (FAZIT), University Hospital Würzburg. Additionally, we recruited a healthy adult male control subject.

Clinical examination and pain assessment

Patients underwent complete neurological examination and were assessed using the Würzburg Fabry Pain Questionnaire.²⁰ Large fibre neuropathy was excluded by clinical examination and nerve conduction studies of the

sural nerve following a standard procedure. Patients additionally underwent quantitative sensory testing (QST) for sensory profiles²¹ and skin punch biopsy.

Skin punch biopsy and fibroblast cultivation

A 6-mm skin punch biopsy (Stiefel GmbH, Offenbach, Germany) was taken in local anaesthesia from the lateral lower calf of all study participants.²² The skin sample was divided in two 3-mm halves. One half was used for immunohistochemistry and determination of the intra-epidermal nerve fibre density (IENFD).^{23,24} From the second half, dermal fibroblasts were derived.²⁵ Briefly, dermis and epidermis were mechanically separated, and the dermal part was collected in fibroblast cultivation medium [Dulbecco's Modified Eagle Medium, DMEM/F12 + 100 U/ml penicillin 100 µg/ml streptomycin (pen/strep; both: Thermo Fisher Scientific, Waltham, MA, USA) + 10% fetal calf serum (FCS; Merck, Darmstadt, Germany)].

Generation of iPSC

All cell lines were cultivated at 37°C with 5% CO₂ (v/v). iPSC were generated using the StemRNA 3rd Gen reprogramming kit (Reprocell, Beltsville, MD, USA) for all male cell lines (FD-1, FD-2 and Ctrl) and the StemMACS mRNA reprogramming kit (Miltenyi Biotec, Bergisch Gladbach, Germany) for the female Fabry cell line (FD-3²⁶). Human dermal fibroblasts were seeded and transfected with the reprogramming cocktail for 4 (FD-1, FD-2 and Ctrl) or 12 consecutive days (FD-3). Putative iPSC colonies were picked, expanded and characterized (see below). Cells were cultivated on human embryonic stem cell-qualified Matrigel (Corning, Corning, NY, USA) in StemMACS iPS-Brew XF cultivation medium (Miltenyi Biotec) supplemented with 100 U/ml pen/strep (Thermo Fisher Scientific). Cells were passaged twice a week using 2 mM ethylenediaminetetraacetic acid in phosphate buffer saline (Thermo Fisher Scientific; Merck) adding 10 µM Y27632 (Miltenyi Biotec) for the first 24 h after splitting and daily change of medium.

iPSC characterization

iPSC clones were extensively characterized.²⁶ Putative iPSC were analysed for the expression of the pluripotency-associated markers octamer-binding transcription factor 4 (OCT4, Santa Cruz Biotechnology, Dallas, TX, USA), TRA-1-60 (Millipore, Burlington, MA, USA) and stage-specific embryonic antigen-4 (SSEA4, R&D Systems, Minneapolis, MN, USA) using immunocytochemistry, with the latter two additionally analysed by flow cytometry with suitable isotype antibodies (all: Miltenyi Biotec) and unstained controls. To prove pluripotency, iPSC were differentiated into cells of all three germ layers using the StemMACS Trilineage Differentiation kit (Miltenyi Biotec). Briefly, iPSC

were seeded and cultivated with chemically defined medium driving differentiation into each germ layer. Cells were analysed via immunocytochemistry for the expression of smooth muscle protein 22-alpha (SM22A, Abcam, Cambridge, UK), ectodermal paired box 6 and SRY-box transcription factor 2 (PAX6/SOX2, Biolegend, San Diego, CA, USA/R&D Systems) and forkhead box protein A2 (FOXA2, Santa Cruz Biotechnology) to verify mesodermal, ectodermal and endodermal identity. To exclude chromosomal aberrations, karyotypes were evaluated using G-banding (FD-1, FD-2: Cell Guidance Systems, Cambridge, UK; FD-3: Creative Bioarray, Shirley, NY, USA; Ctrl: Institute for Human Genetics, University of Würzburg). Mutation analysis was done using polymerase chain reaction (PCR) and Sanger sequencing (Eurofins Genomics, Ebersberg, Germany). GLA activity in iPSC was determined using the Alpha-Galactosidase Activity Assay Kit (Abcam) at 42°C. Supernatant from iPSC was regularly screened for *Mycoplasma* DNA contamination via PCR.

Isogenic Fabry cell line

We generated an isogenic Fabry cell line from the healthy control (ISO-FD) as a result of clustered regularly interspaced short palindromic repeats (CRISPR)/CRISPR-associated protein 9 (CRISPR/Cas9)-mediated random indel mutations following non-homologous end joining.²⁷ A single-guide RNA targeting *GLA* exon 7 was designed using the CHOPCHOP web tool²⁸ and cloned into a plasmid carrying *Streptococcus pyogenes* Cas9 fused to 2A-GFP [pSpCas9(BB)-2A-GFP, Addgene, Watertown, MA, USA]. The construct was transfected into iPSC using Lipofectamine Stem Transfection Reagent (Thermo Fisher Scientific). GFP-positive cells were isolated via fluorescent activated cell sorting to obtain monoclonal lines and screened for successful gene editing by substrate staining with labelled Shiga toxin 1, subunit B (STxB) and Sanger sequencing. To verify enzyme dysfunction, GLA activity was measured. To ensure post-editing integrity of ISO-FD iPSC, basic characterization comprising pluripotency marker expression, three-germ-layer differentiation and karyotype analysis was repeated.

Immunoreaction and expansion microscopy

Immunoreactions were performed following established protocols and depending on target location, cell type and sample type. In brief, samples were fixed with 4% paraformaldehyde (Electron Microscopy Sciences, Hatfield, PA, USA), blocked and permeabilized, if applicable, incubated with primary antibodies overnight, immunoreacted with matching secondary antibodies and mounted for analysis. Fluorescent image acquisition and post-processing followed determined rules (Supplementary Methods). Expansion microscopy was performed following published protocols

(Supplementary Methods and Figs 1 and 2).^{29,30} For a list of antibodies, see Supplementary Table 1.

Sensory neuron differentiation

Following a published protocol,³¹ iPSC on Day -2 were dissociated and seeded into growth factor reduced Matrigel-coated (Corning) six-well plates with a density of 120 000 cells/cm² and cultivated for 2 days adding 10 µM Y27632 for the first 24 h and daily medium changes. On Day 0, medium was switched to KO medium [KSR; KO DMEM/F12 + 2 mM GlutaMAX + 15% KO serum replacement + 100 µM 2-mercaptoethanol + 0.1 mM minimum essential medium non-essential amino acids + 100 U/ml pen/strep (all: Thermo Fisher Scientific)], spiked with a two-inhibitor cocktail (2i) containing 100 nM LDN-193189 (STEMCELL Technologies, Vancouver, Canada) and 10 µM SB-431542 (Miltenyi Biotec). Starting from Day 2, medium was supplemented with 2i and additionally a three inhibitor (3i) cocktail [10 µM SU-5402, 10 µM N-[N-(3, 5-difluorophenacetyl)-l-alanyl]-s-phenylglycine-butyl ester (both: Sigma Aldrich, St. Louis, MO, USA) and 3 µM CHIR-99021 (Axon Medchem, Groningen, the Netherlands)]. Starting at Day 4, KSR medium was replaced by N2 medium [N2; DMEM/F12 GlutaMAX + 1X B-27 Plus Supplement + 1X N-2 Supplement + 100 U/ml pen/strep (all: Thermo Fisher Scientific)], supplemented with 2i + 3i in 25% increments every 2 days until Day 10. On Day 10, cells were washed, detached with TrypLE Express (Thermo Fisher Scientific), centrifuged and seeded in growth factor reduced Matrigel-coated 6-well plates, or 24-well plates with a 1:2 or 1:2.5 ratio, respectively, in neuronal maturation medium (N2 medium + 20 ng/ml brain-derived neurotrophic factor (BDNF) + 20 ng/ml glial cell line-derived neurotrophic factor (GDNF) + 20 ng/ml nerve growth factor, beta subunit (NGFb) [all: PeproTech, Rocky Hill, NJ, USA] + 200 ng/ml ascorbic acid [Sigma-Aldrich, St. Louis, MO, USA]), spiked with 10 µM floxuridine (FdU, Santa Cruz Biotechnology) to reduce residual proliferative cells. Half of the medium was changed once a week, depending on consumption. Neurons were cultivated for ≥5 weeks before analysis ('mature neurons'). Where applicable, neurons were detached using TrypLE Express (Thermo Fisher Scientific) and replated into the required culture vessel using conditioned and fresh media with a 1:1 ratio and addition of FdU. Time in culture between replating and functional analysis was 1 week.

Sensory neuron treatment

Mature neurons were incubated with 1.32 µg/ml agalsidase-beta³² (AGAL; Sanofi Genzyme, Cambridge, MA, USA) for 24 h and were analysed to assess Gb3 load. Neurons were immunoreacted with βIII-tubulin (TUJ1, Abcam) and STxB::555. Coverslips were scanned with a DMi8 fluorescence microscope (Leica Microsystems, Wetzlar, Germany). TUJ1⁺ cells were counted using the cell counter plugin for ImageJ (US National Institutes of Health,

Bethesda, MD, USA)³³ and analysed for STxB⁺ profiles. Coverslips from ≥ 3 independent differentiations per condition were analysed for each Fabry disease cell clone.

Patch-clamp analysis and characterization of single-neuron encoding

Whole-cell patch-clamp recordings were carried out on 5–8-week-old sensory neurons. All measurements were performed at room temperature (RT) and at 39°C since heat is a main trigger of pain in Fabry disease. Current-clamp recordings served to analyse action potential parameters such as threshold potential, amplitude, half-width and firing frequency. To analyse voltage-gated sodium (Na_v) channel and voltage-gated potassium (K_v) channel characteristics, voltage-clamp recordings were performed. Current densities as well as activation and inactivation kinetics were calculated (Supplementary Methods). To assess stimulus-encoding characteristics of single neurons, linear–nonlinear model and generalized linear point process model (GLM) were fit to action potential trains elicited by current-clamp stimulation with broad spectrum Gaussian noise.

Gene expression analysis

Total RNA was extracted using miRNeasy mini kit (Qiagen, Hilden, Germany). 250 ng of RNA was reverse transcribed with MultiScribe reverse transcriptase (Thermo Fisher Scientific). Quantitative real-time PCR (qRT-PCR) was performed using gene specific TaqMan probes (all: Thermo Fisher Scientific; see Supplementary Table 2) with 8.75 ng cDNA as template for targets and endogenous control, in a duplex PCR approach on a QuantStudio 3 qPCR machine (Thermo Fisher Scientific). Data were analysed using the $2^{(-\Delta\Delta C_t)}$ method, normalizing expression of markers in Ctrl-iPSC to 1 and calculating the relative gene expression accordingly, using *GAPDH* as housekeeping gene.

Human Voltage-Gated Ion Channel array plates (Thermo Fisher Scientific) were loaded with pooled cDNA from two clones with two differentiations (FD-1, FD-2 and Ctrl) or one clone with two differentiations (ISO-FD). Each well contained 9.26 ng cDNA, and the reactions were performed on a QuantStudio 3. Data were quantified via ExpressionSuite Software (Thermo Fisher Scientific) using the combined expression values of endogenous controls *18S*, *GAPDH*, *GUSB* and *HPRT1* for ΔC_t normalization. Auto-threshold was applied for all targets based on the combined runs of all arrays, and a cut-off $C_t \geq 33$ was used to determine absence of a respective transcript. Expression is either depicted as ΔC_t or normalized to Ctrl neurons (relative expression, log2fold change). Principle component analysis was carried out via ClustVis³⁴ with relative expression as input at default parameters.

X-chromosome inactivation analysis and *GLA* transcription

X-chromosome inactivation (XCI) was analysed using HhaI digestion, subsequent amplification and fragment analysis (Supplementary Methods).

Ca²⁺ imaging

Mature neurons were loaded with 2 μM Fluo-8 AM (Abcam) for 1 h at 37°C and washed with conditioned neuronal medium. Images were acquired using a confocal laser scanning microscope (LSM700, Zeiss, Oberkochen, Germany) under physiological conditions utilizing a live-cell acquisition chamber (Tokai Hit, Shizuoka, Japan) with a sampling rate of 0.25 Hz for 8 min. For automated and objective analysis of neuronal activity over time, the image processing software Line Profiler (<https://line-profiler.readthedocs.io/en/latest/>) was used. Line Profiler applies a skeletonized algorithm³⁵ to reduce expanded structures to one pixel width. The remaining pixel coordinates are fitted with a c-spline. This gives an analytical description of the structure's orientation and a suitable approximation for its centre. Line profiles are constructed perpendicularly to the derivative of the c-spline. The average of all line profiles is fitted with a Gaussian function:

$$y = Ie^{\frac{(x-c)^2}{2\sigma^2}} \quad (1)$$

where c denotes the centre of the peak. The standard deviation σ and intensity I are saved in a text file for further evaluation. This process is repeated for each timeframe in all regions of interest and allows conclusions about the difference in activity between Fabry and Ctrl neurons.

Mitochondrial mobility and morphology

To investigate mitochondrial mobility, mature Ctrl neurons were incubated with 1 μM of $\omega\text{-N}_3$ sphinganine (synthesized by J.F.) overnight.³⁶ The next day, cells were washed with maturation medium, and 1 μM BODIPY-PEG₄-DBCO (Jena Bioscience, Jena, Germany) and 100 nM MitoTracker Deep Red (Thermo Fisher Scientific) were added in maturation medium before incubation for 30 min in the incubator.³⁶ Live-cell data were acquired using a Lattice-SIM microscope (Elyra 7, Zeiss) with appropriate laser lines. As control conditions, neurons were only incubated with 1 μM BODIPY and 100 nM MitoTracker Deep Red ('dye control').

Mitochondrial morphology was analysed after Tom20 antibody labelling. Photomicrographs were taken using a THUNDER Imager fluorescence microscope (Leica DMI8, Leica Microsystems) and analysed using ImageJ plugin Shape Descriptor.³⁷ The morphology parameters 'form

factor' and 'aspect ratio' were assessed.³⁸ The form factor for branching was computed according to the formula:

$$\text{Form factor} = \frac{P_m^2}{4\pi A_m} \quad (2)$$

P_m = outline length of mitochondrial area and A_m = mitochondrial area.

The aspect ratio was calculated as the ratio of the major and minor axis of an ellipse equalling the shape of the mitochondrion.

Seahorse assay

Sensory neurons were seeded into Seahorse cell plates (Agilent, Santa Clara, CA, USA) and cultivated for 6 weeks. One hour before measuring, cell media were changed to Seahorse XF medium (Agilent) supplemented with 5.5 mM glucose and 1 mM pyruvate. From this time point, cells were incubated without supply of 5% CO₂. After measurement of baseline respiration, sequential administration of 3 μM oligomycin (Sigma Aldrich) was used to measure coupling efficiency, 1 μM carbonyl cyanide-p-trifluoromethoxyphenylhydrazone (FCCP) (Sigma Aldrich) for spare respiratory efficiency and 2 μM Rotenon (Sigma Aldrich) + 1 μM antimycin (Sigma Aldrich) for intoxication.

Statistical analysis

Data analysis was performed using SPSS Statistics 27 (IBM, Armonk, NY, USA) with appropriate parametric or non-parametric tests, stated in the respective figure legends. To account for repeated measurements (different clones per cell line) in patch-clamp data, a mixed-effects model with Bonferroni-adjusted *post hoc* tests was built. Cell line and temperature were classified as fixed effects and clone nested in cell line as random effect. For mixed-effects modelling and pairwise comparison, we used the packages lme4 and emmeans in R (version 4.3.2; R Core Team, R Foundation for Statistical Computing, Vienna, Austria, 2023). Data were visualized using GraphPad PRISM Version 9.5 (GraphPad Software, Inc., La Jolla, CA, USA).

Results

Clinical characterization

We investigated two men (FD-1 and FD-2) and one woman (FD-3) with genetically confirmed Fabry disease and one man as Ctrl with wild-type (wt) *GLA*. Characteristics of the study participants are summarized in [Supplementary Table 3](#). Both male patients carried pathogenic non-sense variants in *GLA* caused by a base substitution (FD-1) leading to a stop codon or a single-base deletion leading to a frameshift (FD-2). FD-3 was diagnosed with a heterozygous missense variant located deeply within the *GLA* protein and classified as 'buried mutation'.³⁹

FD-1 showed a severe Fabry phenotype with cardiomyopathy, nephropathy and Fabry-associated pain since early childhood. FD-1 also had further signs of Fabry-associated small fibre neuropathy, namely elevated thermal perception thresholds in QST and reduced IENFD of 4.9 fibres/mm (laboratory reference value: 9 ± 3 fibres/mm; [Supplementary Fig. 3](#)). In contrast, FD-2 did not have organ involvement and no signs or symptoms of small fibre neuropathy except for asymptomatic reduction of IENFD to 3.7 fibres/mm ([Supplementary Fig. 3](#)).⁴⁰ FD-3 reported Fabry-associated pain attacks without further clinical signs of small fibre neuropathy. She had normal sensory perception thresholds in QST and normal skin innervation (8.5 fibres/mm). We further investigated Fabry and Ctrl skin cryosections and fibroblasts for Gb3 load using fluorescently labelled STxB.⁴¹ We found dense Gb3 deposits in the dermis and in fibroblasts of all three patients, which were absent in Ctrl ([Supplementary Fig. 3](#)).

During regular follow-up visits in 2021, symptoms and clinical signs had further deteriorated in FD-1 (i.e. 6 years after study inclusion, under AGAL treatment). In FD-2 (i.e. 5 years after study inclusion, without treatment), clinical status was unchanged to baseline visit. FD-3 was lost to follow-up.

Fibroblasts from Fabry patients can be reprogrammed to iPSC retaining genotype and cellular phenotype

FD-1, FD-2 and ISO-FD iPSC lines expressed the pluripotency-associated proteins OCT4, TRA-1-60 and SSEA4 ([Supplementary Fig. 4A](#)). Directed differentiation of all lines into the three germ layers resulted in cells expressing SM22A, FOXA2 or PAX6 and SOX2 ([Supplementary Fig. 4B](#)). TRA-1-60 and SSEA4 expression was additionally analysed by flow cytometry with >75% of all TRA-1-60⁺/SSEA4⁺ cells ([Supplementary Fig. 4C](#)). G-banding showed a normal male karyotype (FD-1, FD-2, Ctrl, ISO-FD; 46, XY) after reprogramming and gene editing, respectively ([Supplementary Fig. 4D](#)). Patient-specific variants in *GLA* were confirmed for FD-1-iPSC (c.1069C > T, p.Q357X; hemizygous) and FD-2-iPSC (c.568delG; p.A190Pfs*1; hemizygous), whereas no variants were found in *GLA* of Ctrl-iPSC ([Supplementary Fig. 4E](#)). In ISO-FD-iPSC, the *GLA* variant c.1091_1093del (p.S364del, hemizygous) was generated by CRISPR/Cas9 gene editing. Additionally, we employed FD-3 iPSCs that were characterized as reported previously.²⁶

Fabry iPSC show persisting Gb3 accumulation only in cells of male patients, while iPSC of a female patient undergo *in vitro* restitution by skewed XCI

While Ctrl-iPSC showed no Gb3 depositions ([Fig. 1A](#)), FD-1-, FD-2- and ISO-FD-iPSC had numerous Gb3

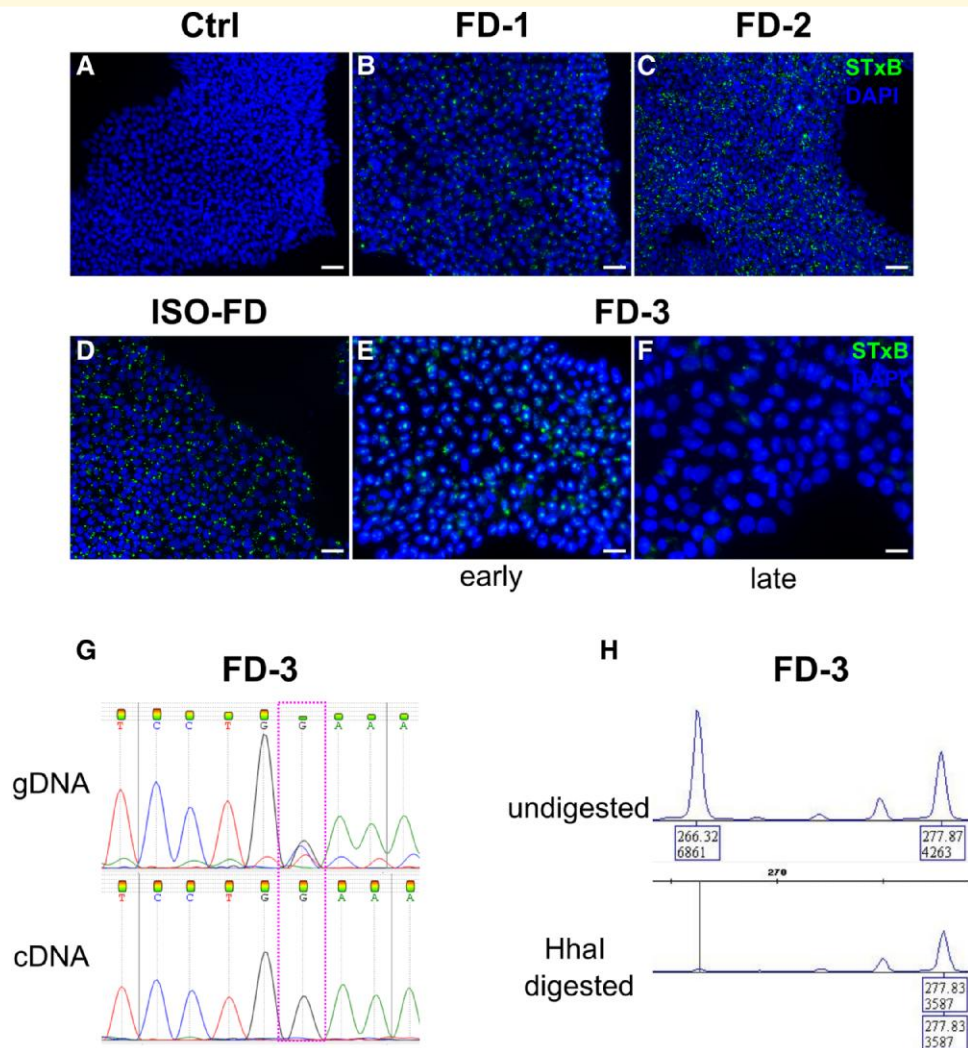


Figure 1 Gb3 accumulations in iPSC and skewed XCI. (A) Ctrl-iPSC show no Gb3 accumulations. Scale bar: 50 μm . (B)–(D) FD-1, FD-2 and ISO-FD iPSC display numerous Gb3 accumulations. Scale bars: 50 μm . (E) iPSC from the female FD-3 line shows Gb3 accumulations in early passages. Scale bar: 25 μm . (F) Gb3 accumulations are lost in iPSC of FD-3 during cultivation (>10 passages). Scale bar: 25 μm . (G) Analysis of gDNA via Sanger sequencing shows the expected heterozygous disease-associated mutation, whereas analysis of cDNA from late FD-3 cells (>10 passages) shows the wild-type sequence. (H) Analysis of X-chromosomal inactivation in late passage (>10 passages) by methylation-sensitive fragment analysis of the polymorphic (CAG)_n repeat in the AR gene. FD-3 cells show a complete shift towards one allele. Ctrl, control; DAPI, 4',6-diamidino-2-phenylindole; FD-1, FD-2, FD-3, patients with Fabry disease; ISO-FD, isogenic Fabry line.

accumulations (Fig. 1B–D). Surprisingly, female FD-3 iPSC displayed Gb3 depositions only in the early (Fig. 1E) but not late phase of cultivation (>passage 10; Fig. 1F). We hence analysed cells for XCI patterns as potential source for the loss of Gb3 during long-term cultivation. *GLA* cDNA sequencing showed the presence of only the wt allele on a transcriptional level in contrast to the genomic level, where both the wt and c.708G>C variant were detected (Fig. 1G). Methylation analysis of the androgen receptor gene (*AR*) revealed a skewed XCI pattern of 0:100, indicating a non-random XCI of one of the parental X-chromosomes rather than a random XCI, where the expected XCI ratio usually follows a 70:30 to 50:50 distribution (Fig. 1H). Since no affected male relative carrying the *GLA* missense mutation was

available for segregation analysis, the polymorphic (CAG)_n repeat sequence of the fully inactivated *AR* allele could not be assigned to the X-chromosome carrying the mutated *GLA* allele or to the wt allele. However, the lack of Gb3 accumulations, the loss of mRNA expression from the mutated allele and the skewed XCI pattern together highly suggest a selective and 100% inactivation of the X-chromosome carrying the *GLA* missense variant. Therefore, FD-3 line was excluded from further experiments.

Mimicking the clinical phenotype, *GLA* enzyme activity was virtually absent in FD-1-iPSC (10.78 nmol/h/mg) and below the assay's detection threshold for FD-2 (<0.006 nmol/h/mg; Supplementary Fig. 4F) compared with normal activity in Ctrl-iPSC (508.98 nmol/h/mg;

Supplementary Fig. 4F). GLA activity was also absent in ISO-FD-iPSC (14.57 nmol/h/mg; Supplementary Fig. 4F) confirming the disrupting effect of CRISPR/Cas9 gene editing on enzyme function.

Functional sensory neurons derived from Fabry iPSC exhibit lysosomal Gb3 deposits cleaved by AGAL

During differentiation, cellular morphology changed to neuron-like cells starting on Day 5. After 10 days, a ganglion-like morphology was visible with non-neuronal cells present (Fig. 2A). Upon splitting and treatment with FdU, the number of non-neuronal cells decreased substantially (Fig. 2B). Immunocytochemistry showed expression of TUJ1 (Fig. 2C), peripherin (PRPH; Fig. 2C), Na_v 1.8 (Fig. 2D), substance P (TAC1; Fig. 2E) and transient receptor potential vanilloid type 1 (TRPV1; Fig. 2F) in mature neurons. Higher expression of neuronal markers *TUJ1*, *PRPH*, *brain-specific homeobox/POU domain protein 3A* (*BRN3A*), *tropomyosin receptor kinase A* (*TRKA*), *islet-1* (*ISL1*), *TRPV1*, *TAC1* and *sodium voltage-gated channel alpha subunit 9* (*SCN9A*) was confirmed in differentiated cells compared with iPSC via qRT-PCR (Fig. 2G). Expression of *SCN10A* was detected in neurons ($C_t < 35$) but not in iPSC ($C_t \geq 35$).

We characterized cellular Gb3 distribution in iPSC and sensory neurons by expansion microscopy and structured illumination microscopy co-applying antibodies against lysosomal-associated membrane protein 1. In Ctrl iPSC, no Gb3 was detected (Fig. 3A), whereas in iPSC of FD-1 (Fig. 3B) and FD-2 (Fig. 3C), numerous intra-lysosomal Gb3 accumulations were present. Quantification of Gb3 accumulations in sensory neurons showed that Ctrl sensory neurons were free of Gb3 accumulations (Fig. 3D and E), while neurons of FD-1, FD2 and ISO-FD showed dense Gb3 depositions (Fig. 3F–H, I and J). Gb3 deposits were cleaved by 27% in FD-1 ($P < 0.001$), 22% in FD-2 ($P < 0.01$) and 16% in ISO-FD ($P = 0.1$) sensory neurons upon 24-h AGAL incubation (Fig. 3D).

Fabry sensory neurons show distinct voltage-gated ion channel expression profiles

iPSC-derived neurons differentiated towards the peripheral lineage were further characterized for mRNA expression patterns of pain-associated voltage-gated ion channels. Micro-array analysis demonstrated that Fabry sensory neuron expression patterns were overall distinct from Ctrl neurons but also showed inter-individual diversity as illustrated by principle component analysis (Fig. 4A). The array revealed an independent signature for sensory neurons of FD-1 who also reported pain, while expression of FD-2 and ISO-FD neurons appeared clustered (Fig. 4A and B). Notably, among the 66/92 (72%) genes detected, *SCN9A*

was expressed highest in all cell lines affirming their sensory nature (Fig. 4B). When analysing cell line signatures, all FD lines shared reduced expression of predominantly voltage-gated potassium channel family members (*KCND2*, *KCNJ11*, *KCNJ4*, *KCNK12*), yet FD-1 differed from both other FD lines and the control as indicated by increased mRNA expression of several channels (*KCNAB2*, *CACNG5*, *SCN3B*, *SCN7A*, *KCNB2*; Fig. 4B and C).

Sensory neurons of FD patients exhibit temperature-dependent hypoexcitability

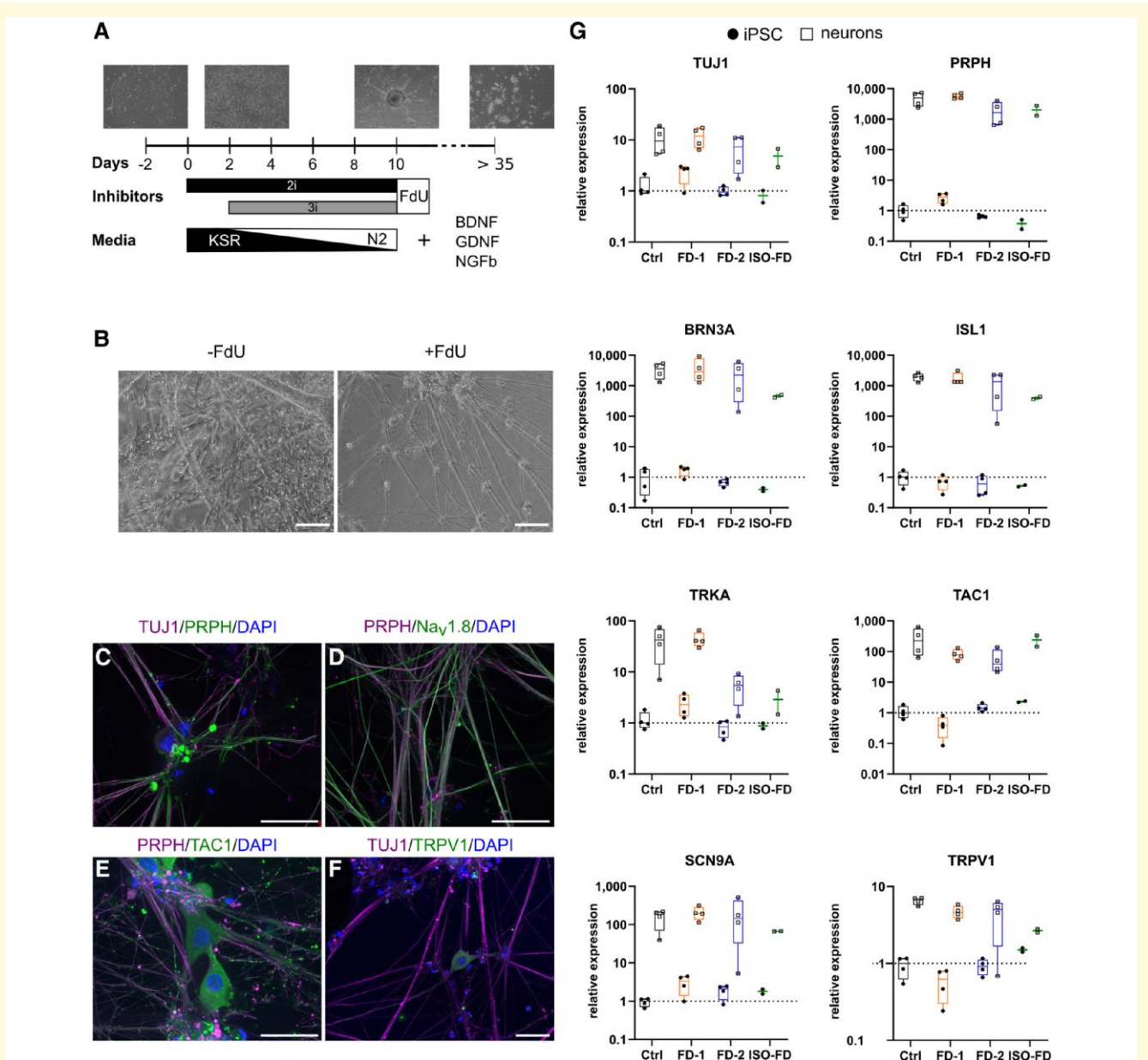
For functional analysis of sensory neurons, we next performed patch-clamp recordings at RT and 39°C as surrogate for clinical fever. Baseline electrophysiological characteristics of the investigated sensory neurons gave similar profiles in all cell lines (Fig. 5A–C; Supplementary Fig. 5A–E). Exposure of neurons to 39°C resulted in increased firing frequencies of action potentials without inter-individual differences (Fig. 5A; Supplementary Fig. 5F). Accordingly, shortening of action potential duration occurred at 39°C as indicated by decreased half-widths ($P < 0.0001$; Fig. 5B) and increased rising slopes ($P < 0.0001$; Fig. 5C).

We next asked whether the cell lines systematically differed in ability to encode time-varying stimuli using linear-nonlinear model and GLM. Action potentials were evoked with a noisy current stimulus (Fig. 5D; Supplementary Methods), and spike-triggered average (STA) currents (Fig. 5E), selectivity for the STA (Fig. 5F) and spike-history effects quantified via GLM analysis were compared (Fig. 5G). All sampled neurons were effectively driven by noisy current patterns and typically integrated current within a 50-ms window. Furthermore, both stimulus and history encoding were markedly temperature dependent.

At RT, the FD-1 population required a larger depolarizing STA (Fig. 5Ei) relative to the other populations. However, at 39°C, both FD cell lines encoded larger depolarizations relative to Ctrl (Fig. 5Eii). Stimulus selectivity, i.e. how precisely spike-evoking stimuli matched the STA, was similar across groups measured at RT, but more variable at 39°C (Fig. 5F). Most strikingly, at 39°C, the FD-1 group was more selective for the STA relative to Ctrl ($P < 0.05$). Moreover, GLM analysis of statistical interactions between spikes revealed that the FD-1 population was ~2–3× more refractory than the other populations at RT (Fig. 5Gi), while these differences largely disappeared at 39°C (Fig. 5Gii).

These data suggest that alterations in both stimulus- and history-encoding properties in FD-1 neurons support a functional decrease in excitability and a sensitivity to temperature, potentially contributing to the clinical hyposensitivity to thermal stimuli determined by QST. In contrast, the FD-2 population showed encoding properties more similar to that of Ctrl.

While sodium current densities were largely unaffected (Supplementary Fig. 5G–J), investigation of steady-state



inactivation curves showed a moderately hyperpolarized shift of inactivation of ISO-FD at RT (Fig. 5H). At 39°C, the negative shift of fast inactivation was even more pronounced in ISO-FD neurons and, to a lesser extent, also present in FD-2 neurons (Fig. 5I). This finding is in accordance

with decreased sodium current availability due to steady-state inactivation. Similarly, $V_{1/2}$ steady-state inactivation was decreased in ISO-FD at 39°C ($P < 0.0001$; Fig. 5J), whereas $V_{1/2}$ in FD-2 was not different from Ctrl. Steady-state activation curves were comparable between all

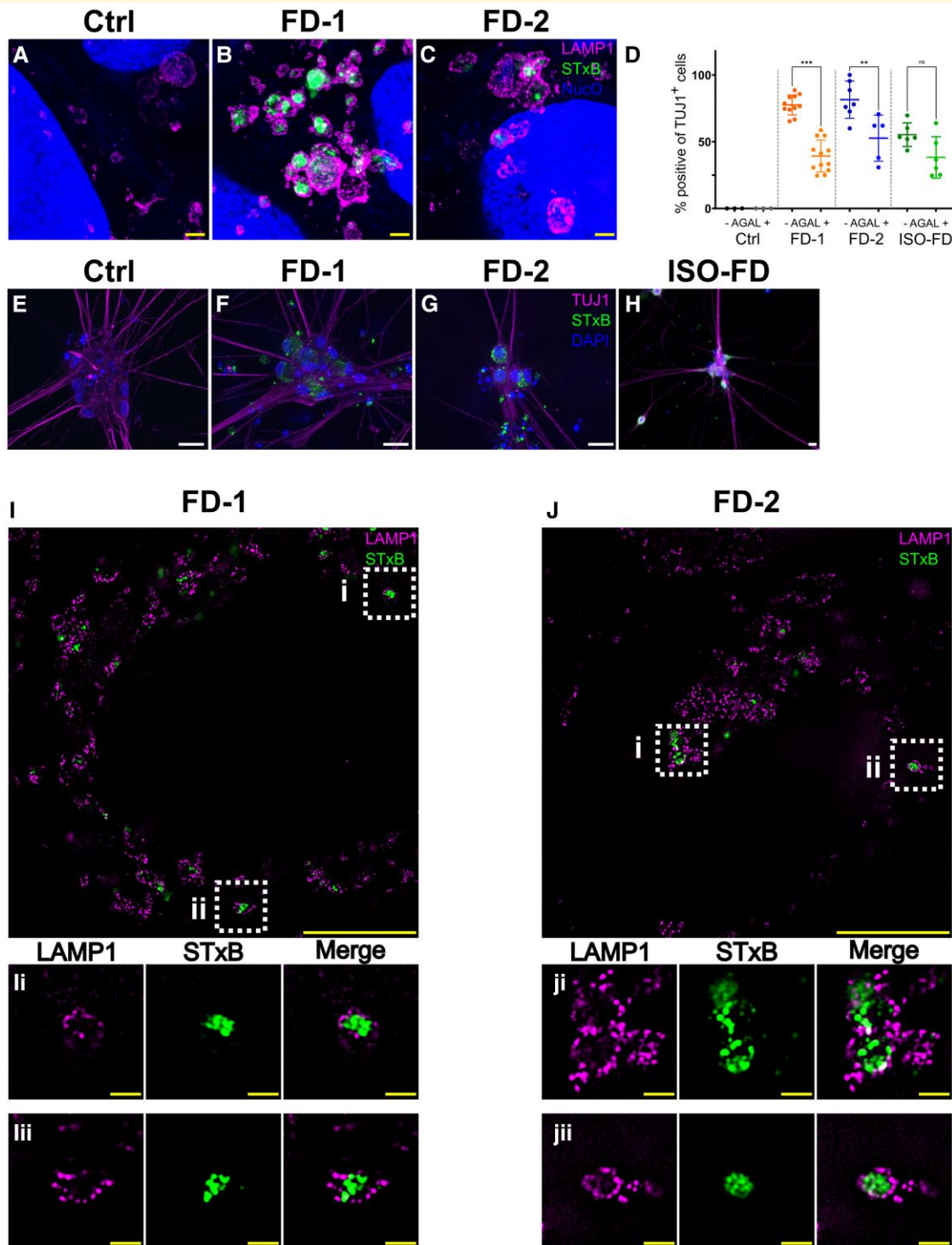


Figure 3 AGAL incubation and in-depth analysis of Gb3 accumulations. (A) Lysosomes of expanded Ctrl-iPSC show no accumulations. Scale bar: 1 μ m (expansion factor corrected). (B) Lysosomes of expanded FD-1 iPSC show prominent intra-lysosomal Gb3 accumulations. Scale bar: 1 μ m (expansion factor corrected). (C) Lysosomes of expanded FD-2 iPSC show prominent intra-lysosomal Gb3 accumulations. Scale bar: 1 μ m (expansion factor corrected). Nuclear orange (NucO) was used to visualize the nuclei; acquired with LSM700 (confocal). (D) Incubation with AGAL reduced Gb3 in FD-1 (untreated: $n = 2$ clones; Clone 1 = 457 cells, Clone 2 = 1050 cells; +AGAL: $n = 2$ clones; Clone 1 = 556 cells, Clone 2 = 1030 cells) and FD-2 (untreated: $n = 2$ clones; Clone 1 = 341 cells, Clone 2 = 300 cells; +AGAL: $n = 2$ clones; Clone 1 = 476 cells, Clone 2 = 150 cells) neurons. AGAL incubation decreased Gb3 deposits also in ISO-FD, although statistics did not reach significance (untreated: $n = 1$ clone, $n = 628$ cells; +AGAL: $n = 1$ clone, $n = 610$ cells). Ctrl neurons did not show any accumulations before ($n = 1$ clone, 150 cells) and after ($n = 1$ clone, 150 cells) AGAL incubation. Each data point represents the mean value of Gb3-positive neurons from one individual coverslip. Data are

(continued)

cell lines at RT (Fig. 5K). At 39°C, steady-state activation of FD-2 and ISO-FD was slightly shifted towards hyperpolarized potentials compared with Ctrl and FD-1 (Fig. 5L). However, $V_{1/2}$ steady-state activation for FD-2, and ISO-FD was similar compared with Ctrl and decreased compared with FD-1 ($P < 0.05$; Fig. 5M). Steady-state activation curves of voltage-gated potassium channels did not show any differences between the cell lines (Supplementary Fig. 5K and L).

Heat increases Gb3-dependent neuronal Ca^{2+} levels and thinning of neurite calibre

We next used confocal Ca^{2+} imaging under physiological (37°C) and clinical fever (39°C; Fig. 6A) conditions and found elevated neuronal Ca^{2+} levels in FD-1 and FD-2 neurons compared with Ctrl neurons already at 37°C ($P < 0.001$; Fig. 6B). At 39°C, Ca^{2+} concentrations further increased dramatically in neurons of both FD cell lines compared with 37°C and with Ctrl neurons ($P < 0.001$ each; Fig. 6B). Interestingly, neurite calibres of FD-1 and FD-2 showed substantial thinning compared with those of Ctrl neurons at baseline ($P < 0.001$; Fig. 6C) and only neurites of FD-1, who reported typical heat-triggered Fabry pain, displayed further thinning upon heat stimulation ($P < 0.001$; Fig. 6C). Neuronal identity was assured by final KCl application leading to excessive Ca^{2+} activity (Video 1).

Fabry sensory neurites exhibit mitochondrial aggregation and altered morphology

While Gb3 can be visualized in fixed cells applying STxB, direct investigation during live cell imaging was not possible. Hence, we used a metabolic, click-chemistry-based labelling approach with the Gb3 precursor ω -N₃-sphinganine (sphinganine).³⁶ Qualitatively, we observed mitochondrial fragmentation and shrinkage in FD sensory neurites mainly in close vicinity to sphinganine accumulations (Fig. 6D), which were absent in dye-control samples (Fig. 6E). In FD-1 neurons, we further observed mitochondrial aggregation at sphingolipid accumulations (Fig. 6F–H; Videos 2–4).

Quantitatively, mitochondria in FD-1 neurons were more branched compared with FD-2, ISO-FD and Ctrl ($P < 0.01$; Fig. 6I), and the aspect ratio was higher in FD cell lines compared with Ctrl ($P < 0.05$; Fig. 6J). Investigation of mitochondrial functionality using Seahorse assays did not show any differences between FD and Ctrl lines regarding oxygen consumption and extracellular acidification rate (Fig. 6K and L). Basal respiration, ATPase-dependent respiration and reserve capacity were also not altered in FD neurons (Fig. 6M–O).

Discussion

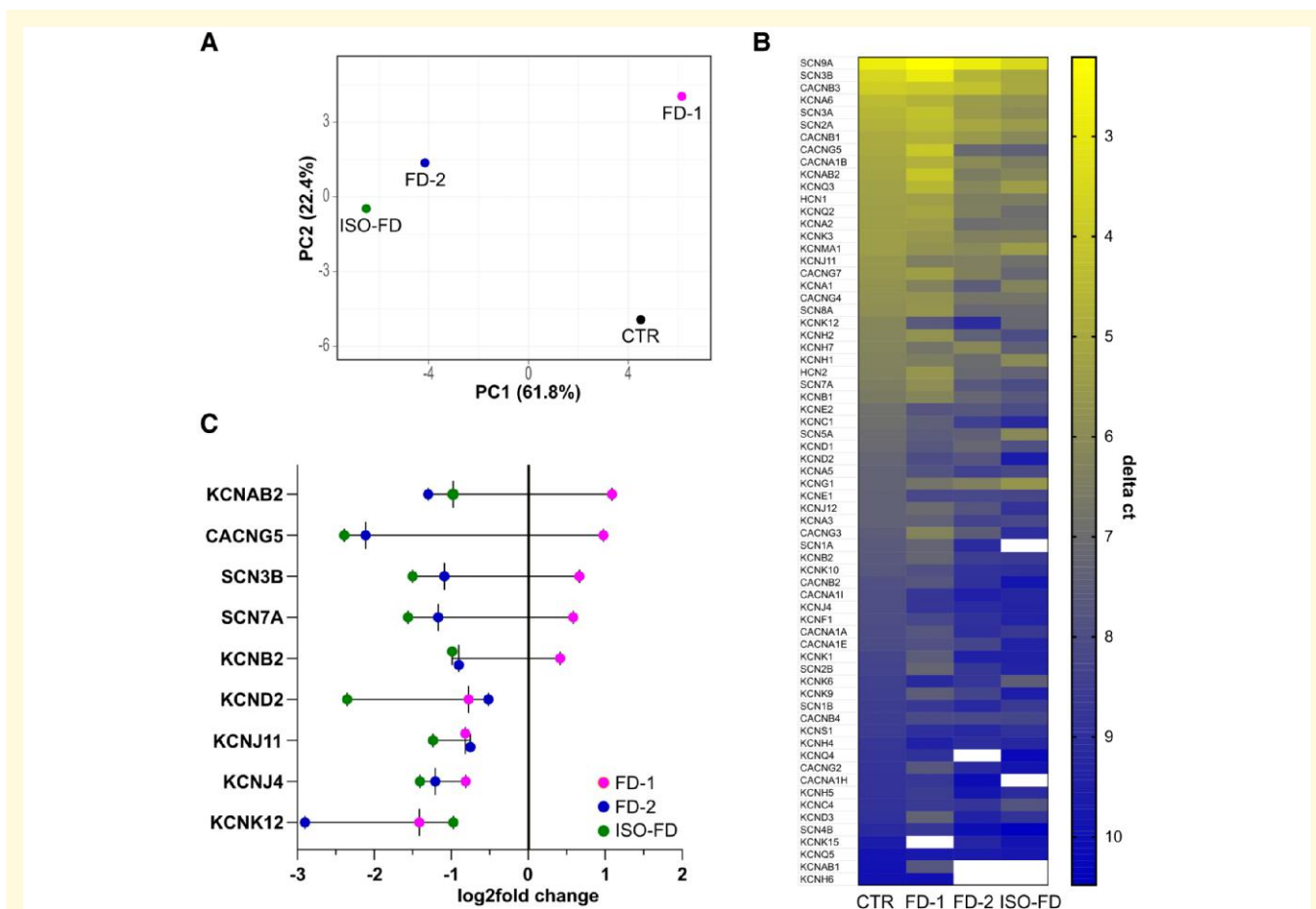
We pioneer the *in vitro* modelling of Fabry disease pathology and provide pilot data linking GLA impairment with small fibre neuropathy in Fabry disease as one of its major clinical hallmarks. We show that sensory neurons derived from iPSC of a patient carrying a non-sense mutation in the *GLA* gene are activated by heat, electrically hypoexcitable and show hints for mitochondrial aggregation within neurites, which may contribute to triggerable neuropathic pain, thermal hyposensitivity and denervation in Fabry disease. Data of our pilot study open novel perspectives for the future study of Fabry disease pain pathophysiology.

Initially, two male patients and one female patient with Fabry disease were included in our study. However, during long-term cultivation of iPSC from the female patient, full skewing of XCI led to a homogenous culture of cells with an active X-chromosome carrying the wt *GLA* gene. We speculate that this gradual loss of mosaicism is caused by a survival advantage of cells carrying an active X-chromosome with the wt *GLA* gene. Such an extreme skewing has already been shown in human embryonic stem cells⁴² and potentially occurs during the cultivation process of hiPSC.

In vitro models have been generated for genetic pain syndromes using iPSC-derived sensory neurons^{15–17,43} and have helped to unravel disease pathophysiology^{15,43,44} and identify novel targets for treatment.^{16,17} In Fabry research, generation of sensory neurons retaining cellular disease phenotype using patient biomaterial was not successful so far,^{45,46} while differentiation of Fabry iPSC to cardiomyocytes,^{11,47} podocytes⁴⁸ or vascular endothelial cells⁴⁹ was achieved. We modified a published differentiation strategy³¹ and

Figure 3 Continued

presented as mean \pm SD. Coverslips from ≥ 3 independent differentiations were used for analysis. One-way ANOVA [$F(7,45) = 34.42$, $P < 0.001$] followed by Sidak's multiple comparison correction. (E) No Gb3 depositions were detected in Ctrl neurons. Scale bar: 25 μ m. (F)–(H) FD-1, FD-2 and ISO-FD-neurons showed massive Gb3 accumulations. Scale bars: 25 μ m. (I) Super-resolution image of an expanded FD-1 neuron showing intra-lysosomal Gb3 accumulations. Scale bar: 5 μ m (expansion factor corrected). (Ii) and (Iii) ROIs cropped from (I). Scale bars: 0.5 μ m (expansion factor corrected). (J) Super-resolution image of an expanded FD-2 neuron showing intra-lysosomal Gb3 accumulations. Scale bar: 5 μ m (expansion factor corrected). (Ji) and (Jii) ROIs cropped from (J). Scale bars: 0.5 μ m (expansion factor corrected). AGAL, agalsidase-beta; Ctrl, control; DAPI, 4',6-diamidino-2-phenylindole; FD-1, FD-2, patients with Fabry disease; Gb3, globotriaosylceramide; ISO-FD, isogenic Fabry line; LAMP1, lysosomal associated membrane protein 1; ROI, region of interest; NucO, nuclear orange; PRPH, peripherin; TUJ1, Class III beta-tubulin. * $P < 0.05$; ** $P < 0.01$; *** $P < 0.001$. For expansion factors, see also Supplementary Figs 1 and 2.



generated iPSC-derived sensory neurons showing pathognomonic Gb3 accumulations. Further, we established an isogenic Fabry cell line generated from healthy control iPSC by CRISPR/Cas9 editing, which showed a comparable GLA enzyme activity with that of patient-derived iPSC. However, due to enhanced apoptosis of ISO-FD sensory neurons especially at 39°C, this cell line could not be included in long-term experiments such as GLM models, Ca^{2+} imaging and Seahorse assay. Increased apoptosis has already been shown in urinary podocytes⁵⁰ as well as in peripheral blood mononuclear cells from Fabry patients⁵¹ and in DRG neurons obtained from a mouse model of Fabry disease,⁶ which also displayed reduced neurite outgrowth compared with neurons of wt mice. Hence, further mechanistic research is needed to clarify the extent and pathophysiological role of neuronal apoptosis and neurite outgrowth in human *in vitro* systems of Fabry disease.

Pain in Fabry disease is one of the very early symptoms starting in childhood⁵² and is mostly episodic and triggerable.^{4,53} Using our *in vitro* disease model, we show that heat, a

typical trigger of Fabry pain, leads to increased Ca^{2+} levels in Fabry neurons, pointing to higher neuronal activity (Fig. 6B). A potential link between Fabry pain and Ca^{2+} levels was already assumed: studies reported alterations of Ca^{2+} -activated ion channel expression in Fabry disease, such as $K_{Ca}1.1$ in patient fibroblasts,⁵⁴ $K_{Ca}3.1$ in Gb3-treated human umbilical vein endothelial cells and aortic endothelial cells from a Fabry mouse model.⁵⁵ Further, elevated intracellular Ca^{2+} concentrations were associated with increased lyso-Gb3 levels, the deacylated derivative of Gb3⁵⁶ in murine DRG neurons leading to pain-related behaviour.¹⁰

We extended knowledge on sensory neuron ion channel RNA expression profiles and found that distinct ion channels were inversely expressed between FD-1 versus FD-2 and ISO-FD neurons. Among these, *KCNAB2* was shown to promote TRPV1 activity,⁵⁷ while *SCN3B* and *SCN7A* were positively correlated with neuropathic or bone pain in animal models.^{58,59} In contrast, *KCNB2* can lead to hyperexcitability when downregulated.⁶⁰ Overall, FD-1 sensory neurons may be tuned towards a more pain promoting

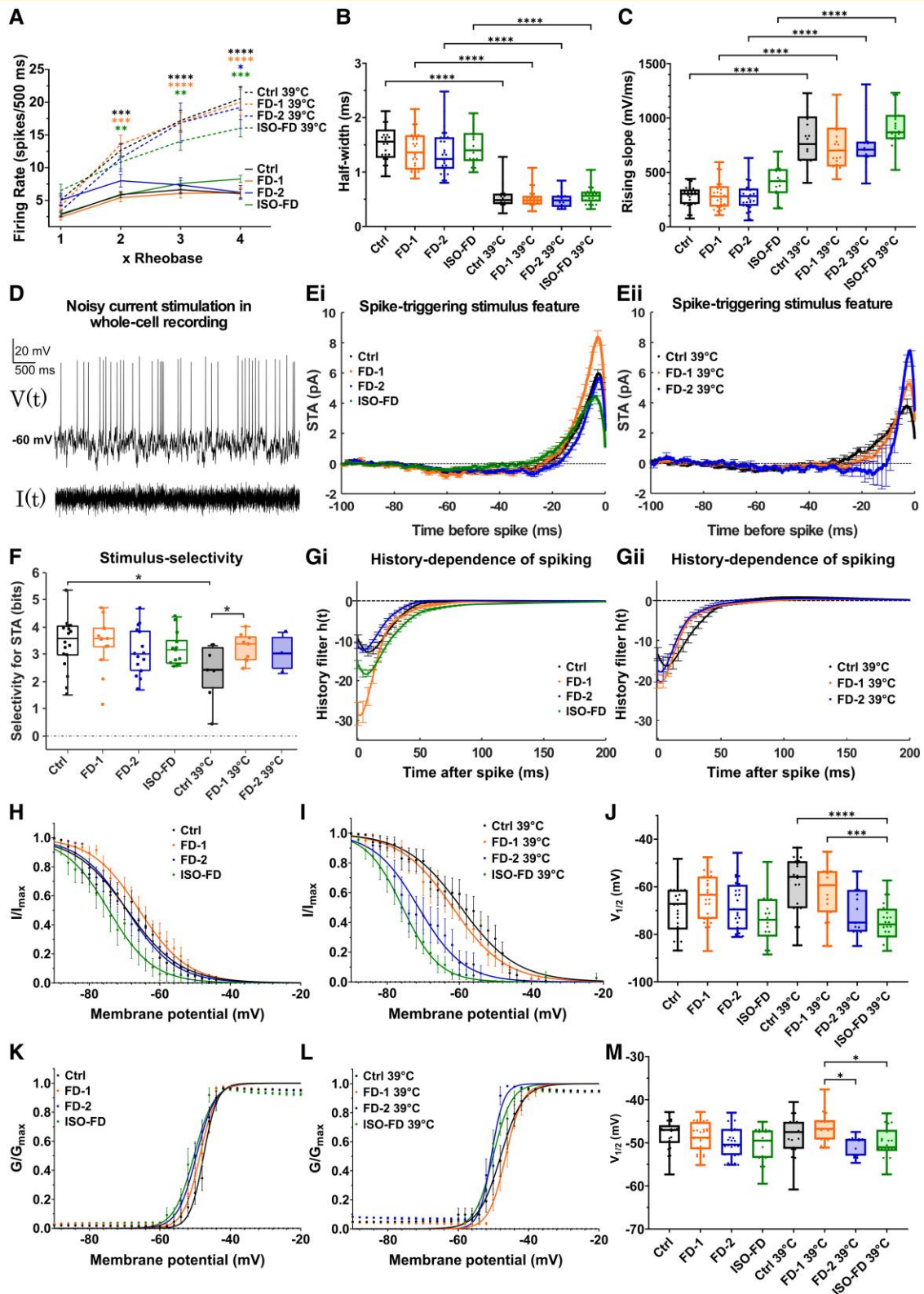


Figure 5 Electrophysiological characterization of sensory neurons. (A) No differences were found in action potential firing rates upon injection of 1x, 2x, 3x and 4x rheabase current between cell lines. Increased firing rates were observed at 39°C compared with RT at 2x and 3x rheabase for Ctrl ($n = 2$ clones; RT: Clone 1 = 7 cells, Clone 2 = 21 cells; 39°C: Clone 1 = 16 cells, Clone 2 = 4 cells), FD-1 ($n = 2$ clones; RT: Clone 1 = 11 cells, Clone 2 = 16 cells; 39°C: Clone 1 = 18 cells, Clone 2 = 5 cells) and ISO-FD ($n = 1$ clone; RT: 19 cells, 39°C: 26 cells) neurons. At 4x rheabase, all cell lines (FD-2: $n = 2$ clones; RT: Clone 1 = 5 cells, Clone 2 = 18 cells; 39°C: Clone 1 = 15 cells) showed increased firing rates at

(continued)

expression profile, matching patients' phenotype, although potential methodological limitations such as variations in the amount of sensory neuron sub-populations between differentiations and clones preclude more detailed conclusions. Further, several voltage-gated potassium channel family members were collectively downregulated in all FD lines and may hint to a partially conserved disease-specific channel expression pattern. Interestingly, Kir6.2 deficiency, encoded by *KCNJ11*, resulted in small fibre dysfunction and axonal degradation in mice.⁶¹

We found thinner neurites of Fabry sensory neurons compared with those of control neurons. Fibre thinning was progressive upon heat simulation exclusively in neurons of FD-1, who also reported pain. Although literature on neurite diameter is sparse, one potential cause for temperature-dependent neuronal shrinkage is hypoxia as shown in ischaemic brains of squirrel monkeys.⁶² We hypothesize that heat leads to increase in neuronal reactive oxygen species in Fabry disease,^{49,63} depleting intracellular oxygen with consecutive cellular shrinkage. Little is known about pain-associated reduction of nerve fibre diameters in the peripheral nervous system; however, there are examples of reduced intra-epidermal nerve fibre calibres, e.g. in fibromyalgia syndrome.⁶⁴ Also, corneal nerve fibre diameter

was reduced in patients with small fibre pathology⁶⁵ correlating with disease severity.⁶⁶ While the exact mechanism remains to be elucidated, reduction of neuronal membrane surface leads to reduced cell capacitance and higher dendritic length constant. This, in turn, facilitates signal propagation and action potential firing,⁶⁷ which may be a contributor to the characteristic heat-triggered Fabry pain phenotype.

Confocal Ca²⁺ imaging enabled the investigation of bulk Ca²⁺ levels in a single focal plane with subcellular resolution, but at the cost of temporal resolution. Still, we show that heat exclusively increases Ca²⁺ levels of Fabry-derived sensory neurons but spares Ctrl neurons, mimicking the triggerable aspect of clinical Fabry pain by fever. The lack of an increased Ca²⁺ signal in Ctrl neurons upon heat stress strongly suggests that Gb3 may be involved in this process.

Age-dependent thermal hyposensitivity is a major symptom particularly in men with Fabry disease. Systematic analysis of warm and cold detection thresholds revealed progressive elevation of perception thresholds even under continued enzyme replacement therapy (ERT).⁶⁸ Studies investigating the *GLA* KO mouse model of Fabry disease showed analogous findings.^{69,70} Electrophysiological recordings gave evidence for reduced sodium current densities in the *GLA* KO mouse model as potentially underlying

Figure 5 Continued

39°C compared with RT. Data are represented as mean ± SEM. Two-way ANOVA [$F(21, 513) = 12.43, P < 0.0001$] followed by Sidak's multiple comparison correction. **(B)** Half-width of action potentials was comparable between all cell lines at RT and 39°C. Reduced half-widths at 39°C for all cell lines compared with RT. Linear mixed-effects model analysis accounting for repeated measurements (different clones per cell line) followed by Bonferroni's multiple comparison correction. Detailed test statistics are given in [Supplementary Table 4](#). **(C)** Rising slope of action potentials was not different between the cell lines at RT and 39°C. Increased rising slopes at 39°C for all cell lines compared with RT. Linear mixed-effects model analysis accounting for repeated measurements (different clones per cell line) followed by Bonferroni's multiple comparison correction. Detailed test statistics are given in [Supplementary Table 5](#). **(D)** Neurons were stimulated with Gaussian white current in patch-clamp whole-cell recordings: voltage response (upper) and noisy stimulus (lower). Representative recording was shown. **(E)** STA illustrates mean current eliciting action potentials calculated via spike-triggered reverse correlation. Positive values indicate depolarizing current; $t = 0$ indicates the time of spiking. At RT, FD-1 neurons required a larger depolarizing STA compared with the other cell lines **(Ei)**. At 39°C, both FD cell lines encoded larger depolarizations compared with Ctrl **(Eii)**. Data are represented as mean ± SEM. **(F)** Stimulus selectivity for STAs shown in **Ei** and **Eii** measured in bits was comparable between the cell lines at RT but increased in FD-1 at 39°C. Large values indicate high selectivity for STA, i.e. the spike-triggering subspace defined by STA is very different from the overall Gaussian stimulus distribution. Rank-sum test. **(G)** History dependence of neuron populations, $h(t)$, calculated via generalized linear model framework (see 'Materials and methods' section) showed a higher refractoriness of FD-1 compared with the other cell lines at RT **(Gi)**, which largely disappeared at 39°C **(Gii)**. Data are represented as mean ± SEM. **(H)** Steady-state inactivation curves of voltage-gated sodium channels at RT. ISO-FD neurons showed negative shift of inactivation compared with Ctrl. Data are represented as mean ± SEM. **(I)** Steady-state inactivation curves of voltage-gated sodium channels at 39°C. FD-2 and ISO-FD neurons displayed negative shift of inactivation compared with Ctrl. Data are represented as mean ± SEM. **(J)** $V_{1/2}$ steady-state inactivation was comparable among Ctrl, FD-1, FD-2 and ISO-FD neurons at RT. However, at 39°C, $V_{1/2}$ was decreased in ISO-FD, and FD-2 showed a trend towards decreased $V_{1/2}$ compared with Ctrl and FD-1. One-way ANOVA [$F(7, 183) = 6.68, P < 0.0001$] followed by Sidak's multiple comparison correction. **(K)** Steady-state activation curves of voltage-gated sodium channels at RT were comparable between the cell lines at RT. Data are represented as mean ± SEM. **(L)** Steady-state activation curves of voltage-gated sodium channels at 39°C displayed a negative shift of FD-2 and ISO-FD compared with Ctrl and FD-1. Data are represented as mean ± SEM. **(M)** $V_{1/2}$ steady-state activation was comparable among Ctrl, FD-1, FD-2 and ISO-FD neurons at RT. At 39°C, $V_{1/2}$ showed a trend towards decreased values for FD-2 and ISO-FD compared with Ctrl. One-way ANOVA [$F(7, 184) = 3.64, P < 0.01$] followed by Sidak's multiple comparison correction. For **(B, C, H–M)**: for Ctrl ($n = 2$ clones; RT: Clone 1 = 8 cells, Clone 2 = 21 cells; 39°C: Clone 1 = 16 cells, Clone 2 = 4 cells), FD-1 ($n = 2$ clones; RT: Clone 1 = 15 cells, Clone 2 = 16 cells; 39°C: Clone 1 = 18 cells, Clone 2 = 5 cells), FD-2 ($n = 2$ clones; RT: Clone 1 = 11 cells, Clone 2 = 18 cells; 39°C: Clone 1 = 15 cells) and ISO-FD ($n = 1$ clone; RT: 19 cells, 39°C: 26 cells) pooled data obtained from ≥3 individual differentiations were used. For **(D–G)**: group sizes for RT and (39°C) were $n = 18$ (7), 14 (9), 15 (3) and 13 (4) for Ctrl, FD-1, FD-2 and ISO-FD, respectively. Data were pooled from two clones per cell line (exc. ISO-FD). For **(B, C, F, J and M)**: each data point represents measurement of one cell. Data are represented as box-and-whisker plots with dots as individual values. The box width indicates the first and third quartiles, the line indicates the median and the whiskers of the box plot indicate the smallest and largest values. Ctrl, control; FD-1, FD-2, patients with Fabry disease; ISO-FD, isogenic Fabry line. * $P < 0.05$; ** $P < 0.01$; *** $P < 0.001$; **** $P < 0.0001$.

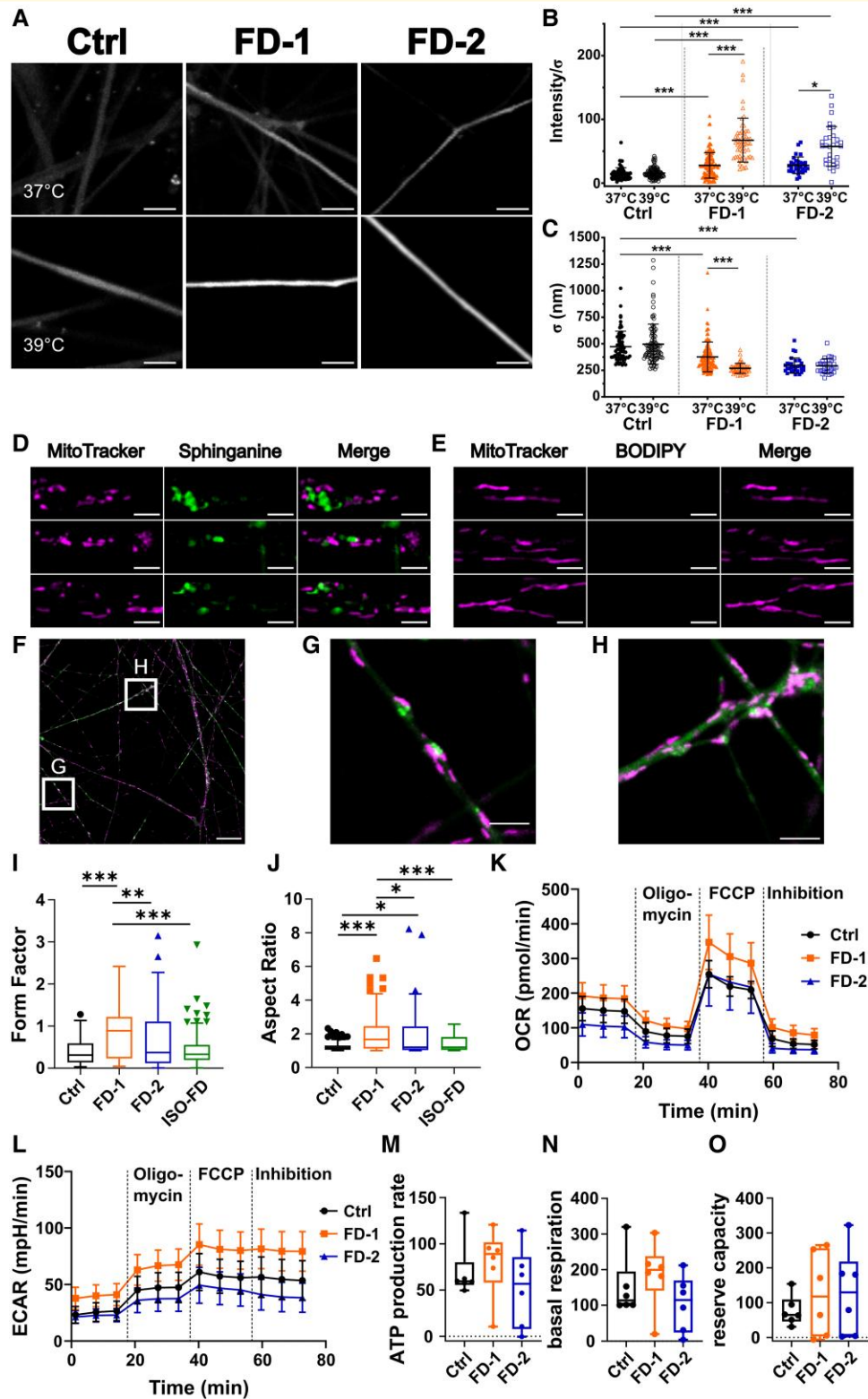


Figure 6 Sensory neuron heat stimulation and mitochondrial characteristics. (A) Exemplified micrographs from firing neurons at 37°C (upper row) and 39°C (lower row). Scale bars: 5 μm. (B) FD-1 and FD-2 neurons show higher activity at 37°C (FD-1: *n* = 1 clone, 179 neurites; FD-2: *n* = 1 clone, 30 neurites) and increased calcium signalling after incubation at 39°C (FD-1: *n* = 1 clone; 56 neurites; FD-2: *n* = 1 clone, 31 neurites), whereas the Ctrl did not show an increase upon heat (37°C: *n* = 1 clone, 63 neurites; 39°C: *n* = 1 clone, 103 neurites). Each data point shows activity of one neurite, and data are represented as mean ± SD. Kruskal–Wallis ($\chi^2 = 181.1$, *P* < 0.0001) followed by Dunn’s multiple comparison test. (C) FD-1 and FD-2 neurons show a generalized decrease in neurite diameter, and FD-1 shows further thinning upon heat stimulation. *n* = 1 clone (B).

(continued)

mechanism, which was Gb3- and age-dependent.⁶ Using extensive electrophysiological analysis including GLM analysis on iPSC-derived sensory neurons, we now show a negative shift of fast steady-state inactivation of voltage-gated sodium channels in the isogenic control cell line, and FD neurons needed larger STA current in accordance with higher inactivation (Fig. 5). It is known that a negative fast inactivation shift leads to pain alleviation,⁷¹ a common mechanism utilized in Na_v channel blocker-based analgesics,⁷² which makes our finding highly interesting for potential druggable targets in analgesic treatment of Fabry pain. In an *in vitro* GLA KO model, we showed that Gb3 directly reduces Na_v1.7 current densities, which can be rescued by AGAL treatment.⁶ We speculate that elevated inactivation of sodium channels may underlie reduced warm and cold perception typically found in Fabry patients. To decipher the subcellular mechanism linking Gb3 deposits with the observed functional alterations in voltage-dependent sodium channels, further studies are needed. In our previous study,⁶ we showed that Na_v1.7 electric properties were altered in GLA KO mice, although its protein expression was unaffected. Therefore, future investigations using our human *in vitro* system should not only focus on expression profiles but also on membrane localization and cytosolic transport of pain-relevant ion channels. While the cellular function of the membrane lipid Gb3 is still unknown, its mere increase might already account for membrane disturbance as was shown in Fabry fibroblasts.⁷³ Hence, an impact of Gb3 on channel clustering⁷⁴ or membrane anchoring could also induce the detected abnormalities.

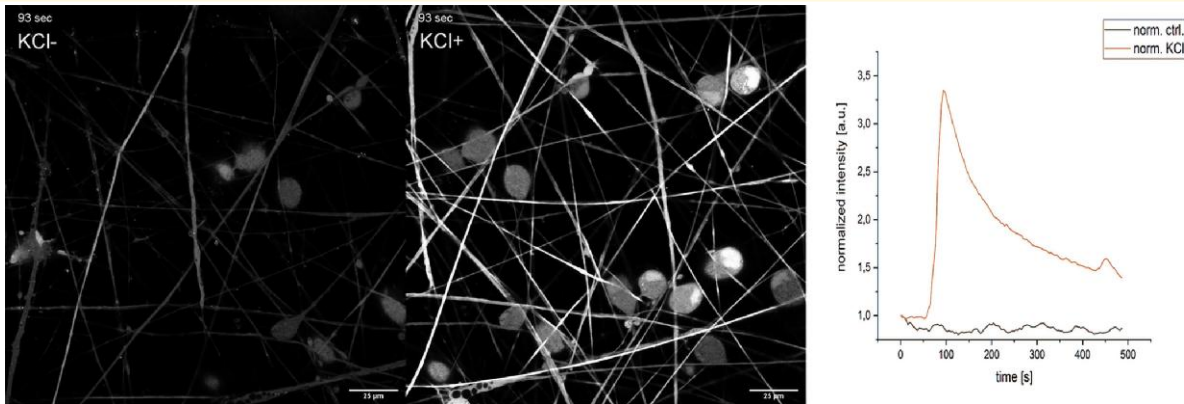
In contrast to our *in vitro* findings, continued ERT does not improve thermal detection thresholds in Fabry patients,⁶⁸ which may be explained by a better response of rejuvenated cells during iPSC generation compared with adult cells

in vivo with chronic Gb3 overload.^{75,76} Besides iPSC-specific effects, it is unclear if and to which extent ERT crosses the blood–nerve barrier *in vivo*.⁷⁷ In our *in vitro* model, nociceptors lack the components typically found in the blood–nerve barrier, such as endoneurial endothelial cells, which limit the transport of proteins into the DRG.⁷⁸ Instead, AGAL can directly enter the neuron, likely via the mannose-6-phosphate receptor.⁷⁹ Analysis of tissue from a deceased Fabry patient revealed that Gb3 accumulations were abundant in all organ systems including the DRG despite ERT.⁸⁰ This further hints to an insufficient permeability of the blood–nerve barrier for ERT, potentially explaining the differences between the *in vivo* and *in vitro* situation.

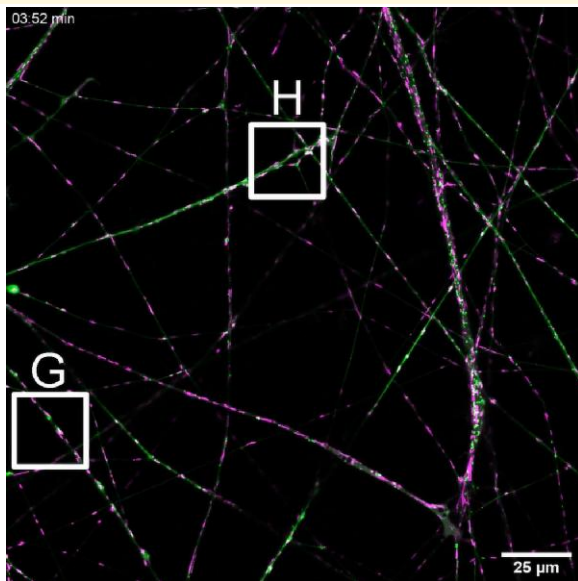
Another characteristic of Fabry disease is peripheral denervation as reflected by reduced IENFD in skin punch biopsies.^{68,81} Using metabolic labelling, we observed mitochondrial aggregation at sphinganine deposits in neurites, which may contribute to dying-back peripheral denervation. However, to draw a definite conclusion on the dynamics of mitochondria, a comprehensive analysis using appropriate tools is warranted. We further found mitochondrial dysmorphisms in Fabry sensory neurons. There is growing evidence for impaired mitochondrial function in lysosomal storage disorders including Fabry disease.⁸² Mitochondrial dysfunction already was linked to neurodegenerative diseases such as Alzheimer's disease,⁸³ Parkinson's disease⁸⁴ or amyotrophic lateral sclerosis.⁸⁵ Quantitative metabolic function was not different between FD sensory neurons, as was recently also shown for podocytes.⁶³ Still, our finding of altered mitochondrial morphology is in line with a recent study reporting glucosylceramide accumulations in murine dopaminergic neurons that trigger impaired interaction of mitochondria and lysosomes and mitochondrion depletion in neurites.⁸⁶

Figure 6 Continued

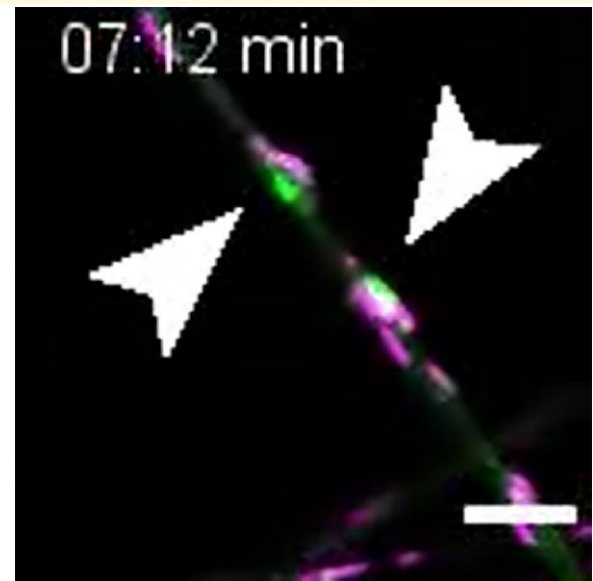
Each data point shows diameter of one neurite, and data are represented as mean ± SD. Kruskal–Wallis ($\chi^2 = 173.1$, $P < 0.0001$) followed by Dunn's multiple comparison test. **(D)** Metabolic labelling with sphinganine in Ctrl neurons reveals mitochondrial fragmentation in the vicinity of accumulations. Scale bars: 2 μm . **(E)** In contrast, incubation of Ctrl neurons with BODIPY only shows normal mitochondrial morphology. Scale bars: 2 μm . **(F)** Still image of mitochondria tracking of FD-1 neurons. Scale bar: 25 μm . **(G)** Still image of mitochondria/sphinganine interaction. Scale bar: 5 μm . **(H)** Still image of potential mitochondrial block by sphinganine. Scale bar: 5 μm . **(G) + (H)** Cropped from **(F)**. **(I)** FD-1 neurons show mitochondria with an increased form factor compared to all other cell lines. Kruskal–Wallis ($\chi^2 = 36.8$, $P < 0.0001$) followed by Dunn's multiple comparison test. **(J)** FD-1 and FD-2 neuronal mitochondria show an increased aspect ratio compared with Ctrl. Aspect ratio of FD-1 neuronal mitochondria is increased compared with FD-2. Kruskal–Wallis ($\chi^2 = 35.41$, $P < 0.0001$) followed by Dunn's multiple comparison test. For **(I) + (J)**: pooled data from $n = 2$ clones/line, obtained from three individual differentiations each was used (20 photomicrographs per differentiation = 60 per clone were analysed). Data are represented as Tukey boxplot. **(K)** Comparison of OCR of Ctrl and FD neurons using Seahorse assay showed no difference in cellular metabolism. Two-way ANOVA [$F(22, 165) = 12.43$, $P = 0.39$] followed by Sidak's multiple comparison correction. **(L)** ECAR was similar between neurons from Ctrl and neurons from FD patients. Two-way ANOVA [$F(22, 165) = 1.52$, $P = 0.07$] followed by Sidak's multiple comparison correction. For **(K–L)**: each data point represents the mean ± SEM of three individual differentiations of $n = 2$ clones/line. **(M)** Seahorse assay showed no difference in ATP production. Kruskal–Wallis ($\chi^2 = 6.75$, $P = 0.08$) followed by Dunn's multiple comparison test. **(N)** No differences in basal respiration. Kruskal–Wallis ($\chi^2 = 7.4$, $P = 0.06$) followed by Dunn's multiple comparison test. **(O)** Reserve capacity was comparable between Ctrl and Fabry patients. Kruskal–Wallis ($\chi^2 = 2.09$, $P = 0.55$) followed by Dunn's multiple comparison test. For **(M–O)**: each data point ($n = 6$) represents measurement of one individual differentiation from one clone. Data are represented as Tukey boxplot. Seahorse assay was performed from three individual differentiations of $n = 2$ clones/line. Ctrl, control; FD-1, FD-2, patients with Fabry disease; ECAR, extracellular acidification rate; FCCP, carbonyl cyanide-p-trifluoromethoxyphenylhydrazone; ISO-FD, isogenic Fabry line; OCR, oxygen consumption rate. * $P < 0.05$; ** $P < 0.01$; *** $P < 0.001$.



Video 1 Neuronal firing induced by KCl incubation. Neuronal activity was induced by application of KCl (right video) compared with non-treated neurons (left video). Normalized intensity was plotted against the acquisition time, and an increase of the calcium indicator dye Fluo 8-AM can be seen in the KCl-treated group after adding at 60 s. Scale bars: 25 μm . KCl, potassium chloride.



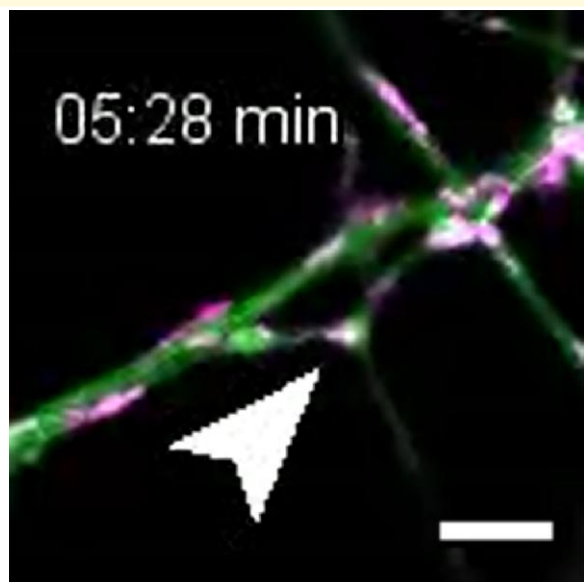
Video 2 Mitochondrial aggregation. Time lapse video of mitochondrial tracking (MitoTracker, purple) after incubation with sphinganine (green) of FD-I neurons hinting to impairment of mitochondrial mobility due to sphinganine accumulations. Scale bar: 25 μm .



Video 3 Mitochondrial aggregation—detailed view 'G'. Detailed view of the region of interest 'G' from Video 2 showing that mitochondria (purple) and sphinganine (green) interact, which may interfere with normal mitochondrial mobility. Scale bar: 5 μm .

We present a patient-specific neuronal and functional human *in vitro* disease model for Fabry disease providing several crucial pilot findings on Fabry pathophysiology: (i) Gb3 accumulates ubiquitously in sensory Fabry neuronal somas and neurites; (ii) lysosomal integrity is impaired displaying a high Gb3 load potentially contributing to fibre degeneration; (iii) pain-related voltage-gated sodium channels from Fabry patients show a differential inactivation kinetic; (iv) neuronal Gb3 accumulations lead to heat-induced Ca^{2+} increase and a decrease in neuronal diameter as potential basis of Fabry pain; and (v) sphingolipid accumulations alter mitochondrial localization and morphology and may

underlie nerve fibre degeneration. However, it should be noted that some of our findings are only attributable to one of the investigated Fabry patients, which hints towards mutation-specific effects. Furthermore, using only one healthy control cell line limits the generalizability of our data. Still, our *in vitro* model opens the avenue to study patient-specific disease mechanisms in a multi-dimensional approach, thus, paving the way towards the development of targeted treatments not only acting on the deficient enzyme itself but also preventing cellular defects as a result of increased neuronal Gb3 load in patients with Fabry disease.



Video 4 Mitochondrial traffic jam—detailed view ‘H’.
Detailed view of the region of interest ‘H’ from [Video 2](#) showing that mitochondria (purple) and sphinganine (green) interact, possibly hindering mitochondrial mobility. Scale bar: 5 μ m.

Supplementary material

[Supplementary material](#) is available at *Brain Communications* online.

Acknowledgements

We thank Daniela Urlaub, Danilo Prtvar, Kathleen Stahl (Department of Neurology, University Hospital Würzburg, Germany) and Birgit Halliger-Keller (Institute for Human Genetics, University of Würzburg, Germany) for expert technical assistance. We further thank our undergraduate students Frederik Bär, Viktoria Diesendorf, Lisa Henkel, Hannah Kiefer, Philipp Neundorf and Maxine Sokolowski (Department of Neurology, University Hospital Würzburg, Germany) for help during cell cultivation. The *Graphical Abstract* was partly generated using Servier Medical Art, provided by Servier, licensed under a Creative Commons Attribution 3.0 unported licence.

Funding

The study was funded by the German Research Foundation (Deutsche Forschungsgemeinschaft, DFG: UE171/3-1 to N.Ü.). Parts of the study were supported by the following: the Interdisciplinary Center for Clinical Research (Interdisziplinäres Zentrum für klinische Forschung, IZKF), University Hospital Würzburg (to N.Ü. and M.S.: project N375); the Collaborative Research Center 1158 funded by DFG (to N.Ü.: project A10); the Research Unit KFO5001

funded by DFG (to N.Ü.: project Z); grants from the European Research Council (ULTRARESOLUTION to J.S., S.R. and M.S.). J.G. (KFO5001), J.S. (RTG2581), N.Ü. (UE171/15-1) and C.M. (Ma 2528/8-1; SFB 1525, project # 453989101) were supported by DFG. K.G. and F.E. received funding from the Austrian Science Fund FWF (M3062-B).

Competing interests

The authors report no competing interests.

Data availability

The data that support the findings of this study are available from the corresponding author, upon reasonable request.

References

1. Brady RO, Gal AE, Bradley RM, Martensson E, Warshaw AL, Laster L. Enzymatic defect in Fabry's disease. Ceramidetrihexosidase deficiency. *N Engl J Med.* 1967;276(21):1163-1167.
2. Germain DP. Fabry disease. *Orphanet J Rare Dis.* 2010;5:30.
3. Schiffmann R. Fabry disease. *Pharmacol Ther.* 2009;122(1):65-77.
4. Üçeyler N, Ganendiran S, Kramer D, Sommer C. Characterization of pain in Fabry disease. *Clin J Pain.* 2014;30(10):915-920.
5. Ohshima T, Murray GJ, Swaim WD, et al. α -Galactosidase A deficient mice: A model of Fabry disease. *Proc Natl Acad Sci USA.* 1997;94(6):2540-2544.
6. Hofmann L, Hose D, Griebshammer A, et al. Characterization of small fiber pathology in a mouse model of Fabry disease. *Elife.* 2018;7:e39300.
7. Lakoma J, Rimondini R, Donadio V, Liguori R, Caprini M. Pain related channels are differentially expressed in neuronal and non-neuronal cells of glabrous skin of Fabry knockout male mice. *PLoS One.* 2014;9(10):e108641.
8. Kummer KK, Kalpachidou T, Kress M, Langeslag M. Signatures of altered gene expression in dorsal root ganglia of a Fabry disease mouse model. *Front Mol Neurosci.* 2018;10:449.
9. Spitzel M, Wagner E, Breyer M, et al. Dysregulation of immune response mediators and pain-related ion channels is associated with pain-like behavior in the GLA KO mouse model of Fabry disease. *Cells.* 2022;11(11):1730.
10. Choi L, Vernon J, Kopach O, et al. The Fabry disease-associated lipid Lyso-Gb3 enhances voltage-gated calcium currents in sensory neurons and causes pain. *Neurosci Lett.* 2015;594:163-168.
11. Itier J-M, Ret G, Viale S, et al. Effective clearance of GL-3 in a human iPSC-derived cardiomyocyte model of Fabry disease. *J Inherit Metab Dis.* 2014;37(6):1013-1022.
12. Oliván-Viguera A, Lozano-Gerona J, López de Frutos L, et al. Inhibition of intermediate-conductance calcium-activated K channel (KCa3.1) and fibroblast mitogenesis by α -linolenic acid and alterations of channel expression in the lysosomal storage disorders, Fabry disease, and Niemann Pick C. *Front Physiol.* 2017;8:39.
13. Chambers SM, Fasano CA, Papapetrou EP, Tomishima M, Sadelain M, Studer L. Highly efficient neural conversion of human ES and iPSC cells by dual inhibition of SMAD signaling. *Nat Biotechnol.* 2009; 27(3):275-280.
14. Wörsdörfer P, Thier M, Kadari A, Edenhofer F. Roadmap to cellular reprogramming—manipulating transcriptional networks with DNA, RNA, proteins and small molecules. *Curr Mol Med.* 2013; 13(5):868-878.

15. Cao L, McDonnell A, Nitzsche A, *et al.* Pharmacological reversal of a pain phenotype in iPSC-derived sensory neurons and patients with inherited erythromelalgia. *Sci Transl Med.* 2016;8(335):335-356.
16. Mis MA, Yang Y, Tanaka BS, *et al.* Resilience to pain: A peripheral component identified using induced pluripotent stem cells and dynamic clamp. *J Neurosci.* 2019;39:382-392.
17. Namer B, Schmidt D, Eberhardt E, *et al.* Pain relief in a neuropathy patient by lacosamide: Proof of principle of clinical translation from patient-specific iPSC cell-derived nociceptors. *EBioMedicine.* 2019; 39:401-408.
18. Li Y, Chan L, Nguyen HV, Tsang SH. Personalized medicine: Cell and gene therapy based on patient-specific iPSC-derived retinal pigment epithelium cells. *Adv Exp Med Biol.* 2016;854:549-555.
19. Chun YS, Byun K, Lee B. Induced pluripotent stem cells and personalized medicine: Current progress and future perspectives. *Anat Cell Biol.* 2011;44(4):245-255.
20. Üçeyler N, Magg B, Thomas P, Wiedmann S, Heuschmann P, Sommer C. A comprehensive Fabry-related pain questionnaire for adult patients. *Pain.* 2014;155(11):2301-2305.
21. Rolke R, Magerl W, Campbell KA, *et al.* Quantitative sensory testing: A comprehensive protocol for clinical trials. *Eur J Pain.* 2006; 10(1):77.
22. Evdokimov D, Frank J, Klitsch A, *et al.* Reduction of skin innervation is associated with a severe fibromyalgia phenotype. *Ann Neurol.* 2019;86(4):504-516.
23. Lauria G, Cornblath DR, Johansson O, *et al.* EFNS guidelines on the use of skin biopsy in the diagnosis of peripheral neuropathy. *Eur J Neurol.* 2005;12(10):747-758.
24. Üçeyler N, Kafke W, Riediger N, *et al.* Elevated proinflammatory cytokine expression in affected skin in small fiber neuropathy. *Neurology.* 2010;74(22):1806-1813.
25. Karl F, Wußmann M, Kreß L, *et al.* Patient-derived in vitro skin models for investigation of small fiber pathology. *Ann Clin Transl Neurol.* 2019;6(9):1797-1806.
26. Klein T, Henkel L, Klug K, Kwok CK, Klopocki E, Üçeyler N. Generation of the human induced pluripotent stem cell line UKWNLi002-a from dermal fibroblasts of a woman with a heterozygous c.608 C > T (p.Thr203Met) mutation in exon 3 of the nerve growth factor gene potentially associated with hereditary sensory and autonomic neuropathy type 5. *Stem Cell Res.* 2018;33: 171-174.
27. Ran FA, Hsu PD, Wright J, Agarwala V, Scott DA, Zhang F. Genome engineering using the CRISPR-Cas9 system. *Nat Protoc.* 2013;8(11):2281-2308.
28. Labun K, Montague TG, Krause M, Torres Cleuren YN, Tjeldnes H, Valen E. CHOPCHOP v3: Expanding the CRISPR web toolbox beyond genome editing. *Nucleic Acids Res.* 2019;47(W1): W171-W174.
29. Chozinski TJ, Halpern AR, Okawa H, *et al.* Expansion microscopy with conventional antibodies and fluorescent proteins. *Nat Methods.* 2016;13(6):485-488.
30. Kunz TC, Götz R, Sauer M, Rudel T. Detection of chlamydia developmental forms and secreted effectors by expansion microscopy. *Front Cell Infect Microbiol.* 2019;9:276.
31. Eberhardt E, Havlicek S, Schmidt D, *et al.* Pattern of functional TTX-resistant sodium channels reveals a developmental stage of human iPSC- and ESC-derived nociceptors. *Stem Cell Reports.* 2015; 5(3):305-313.
32. Schiffmann R, Kopp JB, Austin HA III, *et al.* Enzyme replacement therapy in Fabry disease: A randomized controlled trial. *JAMA.* 2001;285(21):2743-2749.
33. Schindelin J, Arganda-Carreras I, Frise E, *et al.* Fiji: An open-source platform for biological-image analysis. *Nat Methods.* 2012;9(7): 676-682.
34. Metsalu T, Vilo J. ClustVis: A web tool for visualizing clustering of multivariate data using principal component analysis and heatmap. *Nucleic Acids Res.* 2015;43(W1):W566-W570.
35. Lee T-C, Kashyap RL, Chu C-N. Building skeleton models via 3-D medial surface/axis thinning algorithms. *CVGIP: Graph Models Image Process.* 1994;56(6):462-478.
36. Fink J, Schumacher F, Schlegel J, *et al.* Azidosphinganine enables metabolic labeling and detection of sphingolipid *de novo* synthesis. *Org Biomol Chem.* 2021;19(10):2203-2212.
37. Syverud K, Chinga G, Johnsen PO, Leirset I, Wiik K. Analysis of lint particles from full-scale printing trials. *Appita J.* 2007;60(4): 286-290.
38. Mortiboys H, Thomas KJ, Koopman WJH, *et al.* Mitochondrial function and morphology are impaired in *parkin*-mutant fibroblasts. *Ann Neurol.* 2008;64(5):555-565.
39. Rickert V, Wagenhäuser L, Nordbeck P, *et al.* Stratification of Fabry mutations in clinical practice: A closer look at α -galactosidase A-3D structure. *J Intern Med.* 2020;288(5):593-604.
40. Egenolf N, Altenschildesche CM, Kreß L, *et al.* Diagnosing small fiber neuropathy in clinical practice: A deep phenotyping study. *Ther Adv Neurol Disord.* 2021;14:175628642110043.
41. Karmali MA. Infection by verocytotoxin-producing *Escherichia coli*. *Clin Microbiol Rev.* 1989;2(1):15-38.
42. Liu W, Sun X. Skewed X chromosome inactivation in diploid and triploid female human embryonic stem cells. *Hum Reprod.* 2009; 24(8):1834-1843.
43. McDermott LA, Weir GA, Themistocleous AC, *et al.* Defining the functional role of NaV1.7 in human nociception. *Neuron.* 2019; 101(5):905-919.e8.
44. Hameed S. Na_v1.7 and Na_v1.8: Role in the pathophysiology of pain. *Mol Pain.* 2019;15:174480691985880.
45. Kawagoe S, Higuchi T, Otaka M, *et al.* Morphological features of iPSC cells generated from Fabry disease skin fibroblasts using Sendai virus vector (SeVdp). *Mol Genet Metab.* 2013;109(4): 386-389.
46. Miyajima T, Saito R, Yanagisawa H, *et al.* Characterization of cellular phenotypes in neurons derived from induced pluripotent stem cells of male patients with Fabry disease. *J Inherit Metab Dis.* 2023; 46(1):143-152.
47. Birket MJ, Raibaud S, Lettieri M, *et al.* A human stem cell model of Fabry disease implicates LIMP-2 accumulation in cardiomyocyte pathology. *Stem Cell Reports.* 2019;13(2):380-393.
48. Bhuvan T, Wise A, Fuller M, Talbot A, Nicholls K, Ricardo S. SAT-115 generation and characterisation of induced pluripotent stem cells derived from patients with Fabry disease. *Kidney Int Rep.* 2019;4(7):S53-S54.
49. Tseng W-L, Chou S-J, Chiang H-C, *et al.* Imbalanced production of reactive oxygen species and mitochondrial antioxidant SOD2 in Fabry disease-specific human induced pluripotent stem cell-differentiated vascular endothelial cells. *Cell Transplant.* 2017; 26(3):513-527.
50. Fall B, Scott CR, Mauer M, *et al.* Urinary podocyte loss is increased in patients with Fabry disease and correlates with clinical severity of Fabry nephropathy. *PLoS One.* 2016;11(12):e0168346.
51. De Francesco PN, Mucci JM, Ceci R, Fossati CA, Rozenfeld PA. Higher apoptotic state in Fabry disease peripheral blood mononuclear cells: Effect of globotriaosylceramide. *Mol Genet Metab.* 2011;104(3):319-324.
52. Ries M, Ramaswami U, Parini R, *et al.* The early clinical phenotype of Fabry disease: A study on 35 European children and adolescents. *Eur J Pediatr.* 2003;162(11):767-772.
53. Burlina AP, Sims KB, Politei JM, *et al.* Early diagnosis of peripheral nervous system involvement in Fabry disease and treatment of neuropathic pain: The report of an expert panel. *BMC Neurol.* 2011;11:61.
54. Rickert V, Kramer D, Schubert AL, Sommer C, Wischmeyer E, Üçeyler N. Globotriaosylceramide-induced reduction of KCa1.1 channel activity and activation of the Notch1 signaling pathway in skin fibroblasts of male Fabry patients with pain. *Exp Neurol.* 2020;324:113-134.

55. Choi S, Kim JA, Na H-Y, et al. Globotriaosylceramide induces lysosomal degradation of endothelial $K_{Ca}3.1$ in Fabry disease. *Arterioscler Thromb Vasc Biol.* 2014;34(1):81-89.
56. Ferraz MJ, Marques ARA, Appelman MD, et al. Lysosomal glycosphingolipid catabolism by acid ceramidase: Formation of glycosphingoid bases during deficiency of glycosidases. *FEBS Lett.* 2016;590(6):716-725.
57. Bavassano C, Marvaldi L, Langeslag M, et al. Identification of voltage-gated $K(+)$ channel beta 2 (Kvbeta2) subunit as a novel interaction partner of the pain transducer Transient Receptor Potential Vanilloid 1 channel (TRPV1). *Biochim Biophys Acta.* 2013;1833(12):3166-3175.
58. O'Malley HA, Isom LL. Sodium channel β subunits: Emerging targets in channelopathies. *Annu Rev Physiol.* 2015;77:481-504.
59. Ke CB, He WS, Li CJ, Shi D, Gao F, Tian YK. Enhanced SCN7A/Nax expression contributes to bone cancer pain by increasing excitability of neurons in dorsal root ganglion. *Neuroscience.* 2012;227:80-89.
60. Tsantoulas C, Zhu L, Yip P, Grist J, Michael GJ, McMahon SB. Kv2 dysfunction after peripheral axotomy enhances sensory neuron responsiveness to sustained input. *Exp Neurol.* 2014;251:115-126.
61. Nakai-Shimoda H, Himeno T, Okawa T, et al. Kir6.2-deficient mice develop somatosensory dysfunction and axonal loss in the peripheral nerves. *iScience.* 2022;25(1):103609.
62. Little JR, Sundt TM, Kerr J, WF. Neuronal alterations in developing cortical infarction. An experimental study in monkeys. *J Neurosurg.* 1974;40(2):186-198.
63. Braun F, Abed A, Sellung D, et al. Accumulation of α -synuclein mediates podocyte injury in Fabry nephropathy. *J Clin Invest.* 2023; 133(11):e157782.
64. Doppler K, Rittner HL, Deckart M, Sommer C. Reduced dermal nerve fiber diameter in skin biopsies of patients with fibromyalgia. *Pain.* 2015;156(11):2319-2325.
65. Ramirez M, Martinez-Martinez LA, Hernandez-Quintela E, Velazco-Casapia J, Vargas A, Martinez-Lavin M. Small fiber neuropathy in women with fibromyalgia. An in vivo assessment using corneal confocal bio-microscopy. *Semin Arthritis Rheum.* 2015; 45(2):214-219.
66. Brines M, Culver DA, Ferdousi M, et al. Corneal nerve fiber size adds utility to the diagnosis and assessment of therapeutic response in patients with small fiber neuropathy. *Sci Rep.* 2018;8(1):4734.
67. Šišková Z, Justus D, Kaneko H, et al. Dendritic structural degeneration is functionally linked to cellular hyperexcitability in a mouse model of Alzheimer's disease. *Neuron.* 2014;84(5):1023-1033.
68. Üçeyler N, He L, Schönfeld D, et al. Small fibers in Fabry disease: Baseline and follow-up data under enzyme replacement therapy. *J Peripher Nerv Syst.* 2011;16(4):304-314.
69. Üçeyler N, Biko L, Hose D, Hofmann L, Sommer C. Comprehensive and differential long-term characterization of the α -galactosidase A deficient mouse model of Fabry disease focusing on the sensory system and pain development. *Mol Pain.* 2016;12:174480691664637.
70. Lakoma J, Rimondini R, Ferrer Montiel A, Donadio V, Liguori R, Caprini M. Increased expression of Trpv1 in peripheral terminals mediates thermal nociception in Fabry disease mouse model. *Mol Pain.* 2016;12:174480691666372.
71. Emery EC, Habib AM, Cox JJ, et al. Novel SCN9A mutations underlying extreme pain phenotypes: Unexpected electrophysiological and clinical phenotype correlations. *J Neurosci.* 2015; 35(20):7674-7681.
72. Zheng YM, Wang WF, Li YF, Yu Y, Gao ZB. Enhancing inactivation rather than reducing activation of Nav1.7 channels by a clinically effective analgesic CNV1014802. *Acta Pharmacol Sin.* 2018; 39(4):587-596.
73. Brogden G, Shammas H, Maalouf K, et al. Case study on the pathophysiology of Fabry disease: Abnormalities of cellular membranes can be reversed by substrate reduction *in vitro*. *Biosci Rep.* 2017; 37(2):BSR20160402.
74. Zhang J, Carver CM, Choveau FS, Shapiro MS. Clustering and functional coupling of diverse ion channels and signaling proteins revealed by super-resolution STORM microscopy in neurons. *Neuron.* 2016;92(2):461-478.
75. Reisin R, Perrin A, Garcia-Pavia P. Time delays in the diagnosis and treatment of Fabry disease. *Int J Clin Pract.* 2017;71(1):e12914.
76. Mehta A, Ricci R, Widmer U, et al. Fabry disease defined: Baseline clinical manifestations of 366 patients in the Fabry outcome survey. *Eur J Clin Invest.* 2004;34(3):236-242.
77. Vogler C, Levy B, Grubb JH, et al. Overcoming the blood-brain barrier with high-dose enzyme replacement therapy in murine mucopolysaccharidosis VII. *Proc Natl Acad Sci USA.* 2005;102(41): 14777-14782.
78. Ubogu EE. The molecular and biophysical characterization of the human blood-nerve barrier: Current concepts. *J Vasc Res.* 2013; 50(4):289-303.
79. Lee K, Jin X, Zhang K, et al. A biochemical and pharmacological comparison of enzyme replacement therapies for the glycolipid storage disorder Fabry disease. *Glycobiology.* 2003;13(4):305-313.
80. Schiffmann R, Rapkiewicz A, Abu-Asab M, et al. Pathological findings in a patient with Fabry disease who died after 2.5 years of enzyme replacement. *Virchows Arch.* 2006;448(3):337-343.
81. Scott LJC, Griffin JW, Luciano C, et al. Quantitative analysis of epidermal innervation in Fabry disease. *Neurology.* 1999;52(6): 1249-1249.
82. Ivanova M. Altered sphingolipids metabolism damaged mitochondrial functions: Lessons learned from Gaucher and Fabry diseases. *J Clin Med.* 2020;9(4):1116.
83. Swerdlow RH. Pathogenesis of Alzheimer's disease. *Clin Interv Aging.* 2007;2(3):347-359.
84. Wang X, Winter D, Ashrafi G, et al. PINK1 and Parkin target Miro for phosphorylation and degradation to arrest mitochondrial motility. *Cell.* 2011;147(4):893-906.
85. Smith EF, Shaw PJ, De Vos KJ. The role of mitochondria in amyotrophic lateral sclerosis. *Neurosci Lett.* 2019;710:132933.
86. Kim S, Wong YC, Gao F, Krainc D. Dysregulation of mitochondria-lysosome contacts by GBA1 dysfunction in dopaminergic neuronal models of Parkinson's disease. *Nat Commun.* 2021;12(1):1807.